Design of Sand-Based, 3-D-Printed Analog Faults With Controlled Frictional Properties

Philipp Braun, Georgios Tzortzopoulos, Ioannis Stefanou

Design of sand-based, 3D-printed analogue faults with controlled frictional properties

P. Braun[1], **G. Tzortzopoulos**[1], **I. Stefanou**[1]

[1]Institut de Recherche en Génie Civil et Mécanique, Ecole Centrale de Nantes
1 Rue de la Noë, Nantes 44321, France

Key Points:

- We design and test analogue fault interfaces using 3D-printing with sand particles
- We control the evolution of the friction coefficient with slip, by adequately designing the printed interface geometry
- Wear and gouge production is enhanced by adjusting the 3D-printing settings

Corresponding author: Philipp Braun, philipp.braun@enpc.fr

Abstract

Laboratory experiments with surrogate materials play an important role in fault mechanics. They can improve the current state of knowledge by testing various scientific hypotheses in a repeatable and controlled way. Central in these experiments is the selection of appropriate analogue, rock-like materials. Here we investigated the frictional properties of sand-based, 3D-printed materials. Pursuing further recent experimental works, we performed uniaxial compression tests, direct shear and inclined plane tests in order to determine a) the main bulk mechanical parameters of this new analogue material, b) its viscous behavior, c) its frictional properties, and d) the influence of some printing parameters. Complete stress-strain / apparent friction-displacement curves were presented including the post-peak, softening behavior, which is a key factor in earthquake instability. The rate-and-state frictional parameters were also obtained.

Going a step further, we printed rock-like interfaces of custom frictional properties. Based on a simple analytical model, we designed the a) maximum, minimum and residual apparent frictional properties, b) characteristic slip distance, c) evolution of the friction coefficient with slip and d) dilatancy of the printed interfaces. This model was experimentally validated using interfaces following a sinusoidal pattern, which led to an oscillating evolution of the apparent friction coefficient with slip. Our approach could be used for simulating earthquake-like instabilities in the laboratory and mimic the periodical rupture and healing of fault sections. Additionally, our tests showed the creation of a gouge-like layer due to granular debonding during sliding, whose properties were quantified. The experimental results and the presented methodology make it possible to design new surrogate laboratory experiments for fault mechanics and geomechanics.

1 Introduction

The slow movement of tectonic plates continuously accumulates elastic energy in the earth's crust, which is suddenly released during earthquakes. A small part of this energy travels up to the surface in the form of seismic waves, which have catastrophic results for our built and shaped environment (Jones, 2018). Nevertheless, most of the energy is dissipated in the fault zone due to friction. Friction determines the nucleation of an earthquake, the evolution of seismic slip and the magnitude of seismic events (C. Scholz, 2002). Understanding friction is therefore a key element for studying earthquake nucleation, its possible mitigation and control (e.g. Raleigh et al., 1976; Barbot et al., 2012; Popov et al., 2012; Edwards et al., 2015; Bommer et al., 2006; Stefanou, 2019). Central in building understanding of induced/triggered earthquakes and their potential mitigation are in-situ measurements and laboratory testing.

Several experimental approaches have been developed for reproducing earthquakes in the laboratory. Laboratory experiments involve testing of natural rocks or rock-like, surrogate materials (e.g. Brace & Byerlee, 1966; Dieterich, 1979, 1981a; Power et al., 1988). A large variety of analogue materials has been employed in the literature. For instance, we refer to experiments with glass beads (Anthony & Marone, 2005), rubber (Schallamach, 1971), foam rubber (Brune, 1973), sandpaper (King, 1975), cardboard (Heslot et al., 1994), pasta (Knuth & Marone, 2007), and absorbent paper (Tzortzopoulos et al., 2020) , among others (see Rosenau et al., 2017, for a comprehensive overview). Analogue materials permit not only to have better control over different parameters, but also to produce numerous specimens for repeatable experiments. *Repeatability* and *falsifiability* are of paramount importance for testing any theory or conjecture. This is especially important for systems where direct measurements are difficult to obtain or contain multiple sources of error. In this work, we propose a new analogue material for fault experiments, which enables the design of the apparent frictional parameters of rock-like frictional interfaces. This is achieved using 3D-printing with sand particles. This novel approach gives the advantage of controlling several properties such as the roughness, the exact geometry of the asperities, the maximum and minimum apparent friction coefficient, the exact evolution

of friction with slip and the characteristic slip-weakening distance, d_c^{sw}, of the frictional interfaces.

In literature, experiments on rock friction have not only been of interest in fault mechanics, but also in wider geo-engineering applications such as the stability in tunnelling and slopes. One can find a large number of studies discussing the contribution of joint roughness and asperities to the shear resistance of rocks, following the pioneering works of Newland and Allely (1957); Patton (1966). Analogue specimens have been created in this regard, as for instance for investigating the effects of triangle-shaped asperities on the shear resistance (Huang et al., 2002). These authors tested specimens made of a mix of chalk, sand and water, and analyzed the observed asperity friction and asperity cut-off in a theoretical model. Moreover, Asadi et al. (2013); Indraratna et al. (2015) showed experimentally on synthetic rocks, that the joint friction can be significantly reduced by asperity damage.

Analogue interfaces, resembling more closely to the geometry of natural rocks, have been replicated by 3D-printed molds (e.g. Fang et al., 2018) or 3D-printed acrylic resin specimens (Ishibashi et al., 2020). The aforementioned analogue materials permitted to carry out laboratory experiments and to infer properties that occur in real faults. Moreover, they allowed to explore the mechanisms behind various phenomena, such as asperity damage and gouge material creation, and their effect on apparent friction.

Here we go beyond that approach, by taking key fault characteristics and scale them down to the lab scale. These key properties can be local parameters, or average properties of an entire fault area, obtained through geodetic and seismological measurements. We use a recently developed, composite, analogue material, which gives a large scope for adjusting composition and micro-structural behavior of analogue rock-like frictional interfaces. More specifically, we employ sand-based 3D-printing, which enables us to adjust the geometry and roughness of analogue fault interfaces. Using Patton's considerations on roughness (Patton, 1966), we succeed in generating desired frictional properties and reproduce the effects of asperity breakage and fault gouge creation. The latter is possible thanks to the applied 3D-printing technology, which uses sand particles of controlled size connected through resin bonds, that can break during shearing. Moreover, sand-based 3D-printing allows us to control the post-peak characteristic slip-weakening distance d_c^{sw}, which, together with the adjustable maximum and residual friction coefficient, enable us to control the frictional dissipation during slip. Note that this is central in the study of the earthquake phenomenon and its triggering (C. Scholz, 2002; Rattez et al., 2018a, 2018b; Stefanou, 2019).

The paper is organized as follows. In Section 2, we present the employed sand-based 3D-printing technology (S3DP). We characterize the basic mechanical properties of the S3DP material through element tests and investigate how the material composition and printing settings can influence its mechanical behavior. For this purpose, we perform Uniaxial Compressive Strength (UCS) tests on the bulk material and direct shear tests to 3D-printed flat interfaces, for characterizing the frictional properties including the angle of friction and the rate-and-state parameters. Then, in Section 4, we show how the frictional behavior is directly related to the designed geometry of the analogue fault asperities and we validate the predicted frictional behavior through shear experiments on sinusoidal interfaces. Finally, in Section 5, we discuss advantages, shortcomings, and perspectives of our approach for analogue experiments in fault mechanics.

2 3D-printed analogue rock

2.1 3D-printing technology

We use binder-jetting, a sub-category of 3D-printing technologies, for printing desired geometries of rock-like materials. Binder-jetting allows one to create composite ma-

terials by controlled mixing of two components: powder and binder. Among the various potential granular materials, we use here silica sand as the powder component. Before the printing process, silica sand is mixed with an acidic activator. This activator serves later as a catalyst for the polymerization reaction of the binder. As shown in Figure 1a, a recoater and an inkjet head run over the build platform in alternating sequence. First, the recoater deposits a layer of the sand-activator mixture with a thickness of two times the mean grain diameter D_{50} of silica sand (here D_{50} = 140 μm). At the same time, it applies a small vertical pressure, in order to compact the new layer. Then, the inkjet head drops the binder (Furfurylic alcohol), which reacts with the activator and solidifies. Due to capillary forces, the binder is concentrated at the grain contacts and forms solid bridges, resulting in a rigid sand-binder matrix as depicted in Figures 1b,c. Gravitational forces distribute the binder throughout the new sand layer and ensure binding to the previously deposited layer. Controlled amounts of binder are then deposited on each layer, under a given binder-to-sand ratio. Finally, the building platform moves downwards and a new layer is printed, until the desired geometry is completed (for more details on the printing procedure we refer to Primkulov et al., 2017; Gomez et al., 2019; Mitra, Rodríguez de Castro, & El Mansori, 2019). The shape of the final object, which can be of arbitrary geometry (Figure 1d), is defined through an input CAD model. All principal printer settings for creating the specimens tested in this work are presented in Table 1a.

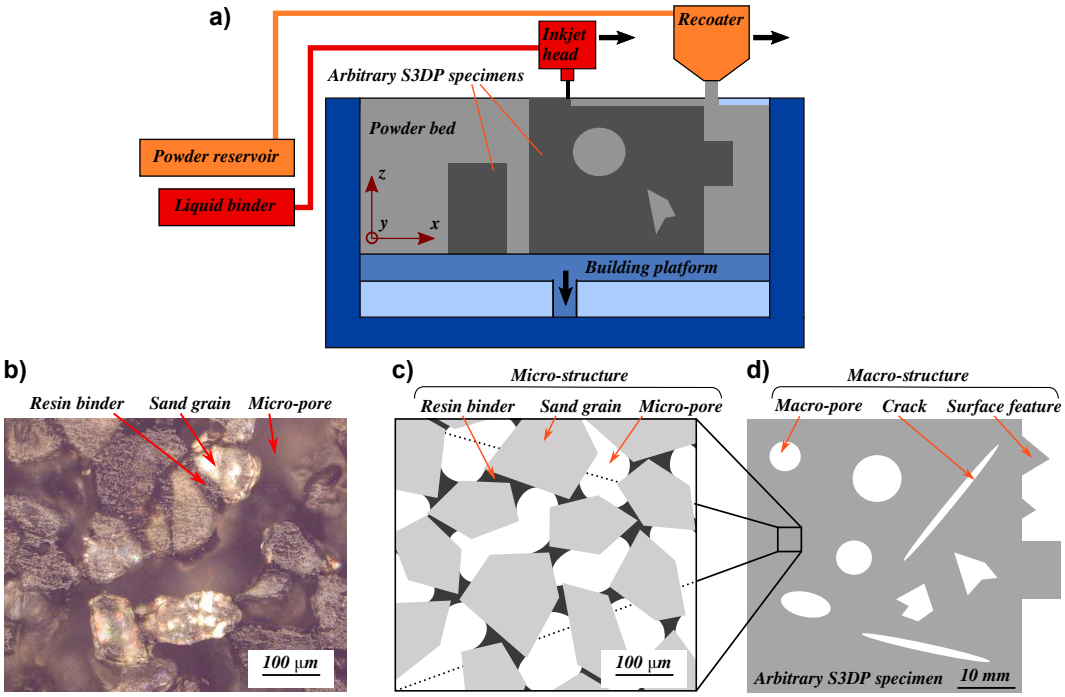

Figure 1. a) Schematic elements of a 3D printer for powder-binder composites, adapted from Upadhyay et al. (2017). b) Cross section of the S3DP material. c) Schematic representation of the micro-structure and d) of the macro-structure of the S3DP material.

2.2 Micro-mechanical properties and analogies with natural rocks

Specimens created by powder-based 3D-printing are characterized by their micro- and macro-structure (Figure 1b-d). The micro-structure describes the composition of the powder, binder and pore phases, and can be adjusted to a large extent to achieve desired

Table 1. a) Printer settings applied for specimen fabrication. b) Compositions for sand printing, representing different combinations of binder content b and recoating speed v_r. The resulting average porosity ϕ and its standard deviation (SD) are given.

(a)

Silica sand mean grain diameter	140 μm
Binder type	Furfurylic alcohol
Binder content	3.8 or 7.2 wt% of sand
Recoating speed	0.13 or 0.26 m/s
x resolution	20 μm$^{(1)}$ or 40 μm$^{(2)}$
y resolution	101.6 μm
z resolution (layer thickness)	280 μm
Activator content (sulfonic acid)	0.2 wt% of sand
Infra-red curing lamp temperature	32 °C

$^{(1)}$ for high and $^{(2)}$ for low binder content

(b)

Composition	b [wt% of sand]	v_r [m/s]	ϕ [%]	SD [%]
R1	3.8	0.13	43.7	0.6
R2	3.8	0.26	47.6	1.0
R3	7.2	0.13	42.8	4.2
R4	7.2	0.26	45.1	2.2

macroscopic mechanical properties. More specifically, the macroscopic mechanical properties of 3D printed analogues based on powder minerals (such as the S3DP material used herein) can be controlled by different process variables. For instance, phase composition, macroporosity and pore geometry have high impact on the compressive strength of 3D-printed specimens (Schumacher et al., 2010). Vaezi and Chua (2011) found that increasing the binder saturation of plaster-powder-based printed materials can improve mechanical resistance. They also observed that an increase of the printing layer thickness reduces the tensile resistance, but increases flexural strength. Moreover, the printing layer orientation induces anisotropy in the microstructure (Vlasea et al., 2015), which can affect the apparent mechanical and hydraulic properties at the macro-scale. While having a minor effect on dimensional accuracy and pore structures, the printing speed can have a significant influence on the strength and structural accuracy of 3D-printed specimens. Farzadi et al. (2015) showed, that very fast printing prevents the binder from spreading and penetrating uniformly, resulting in lower mechanical resistance. Conversely, if printing is carried out too slow, the binder hardens before the subsequent layer is completed, resulting in reduced adhesion between layers, leading to lower resistance. While the binder cures, heating the layer up to a certain temperature can improve the mechanical properties (Primkulov et al., 2017). Very high temperatures, however, can reduce the mechanical resistance. In addition, ageing, curing time and curing temperature can influence S3DP materials (Mitra et al., 2018).

Mechanical properties of S3DP analogues can be adjusted through the most important printing parameters: a) the printing layer thickness, b) the layer orientation and c) the binder saturation (Gomez et al., 2019). According to Gomez et al. (2019), the printing layer thickness defines the thickness of new material added parallel to the building plane in each printing step. The layer orientation describes the angle between printing layers and loading direction, while the binder saturation denotes the percentage of sand

pore volume filled by binder. Moreover, Gomez et al. (2019) have found an increase of uniaxial compressive strength with increasing binder saturation. On the contrary, when they increased the layer thickness from 220 to 400 μm, they measured a significant decrease of uniaxial compressive strength. Finally, Mitra, Rodríguez de Castro, and El Mansori (2019) noted that a higher recoating speed leads to a lower grain packing density and therefore higher porosity. Furthermore, heterogeneities in density might increase due to the faster distribution of sand.

Even though literature examples of the use of sand-based 3D-printed materials in geomechanics applications are limited, Gomez (2017); Gomez et al. (2019) state that for given sand and binder properties, S3DP materials show similar behavior and mechanical characteristics with natural rocks. For instance, they measured an unconfined compressive strength between approximately 15 and 20 GPa, a Young modulus between 1.6 and 1.9 GPa and a Poisson ratio between 0.19 and 0.25 on S3DP specimens with a porosity between 36 and 47%. Their cylindrical specimens had dimensions of 38.1 mm diameter and 76.2 mm height, and 63.5 mm diameter and 127 mm height, respectively (compared to our samples of 20 mm diameter and 40 mm height). These mechanical properties are close to the ones found on weak sandstones, such as the Wildmoor or Waterstone sandstones (compressive strength of approximately 10 and 20 GPa, Young's modulus of around 2 and 7 GPa, porosity of 25%, respectively, according to Dobereiner & Freitas, 1986; Papamichos et al., 2000).

Intact crustal rocks can have a large range of stiffness (Young's modulus up to tens of GPa), while the stiffness of the rock material in a fault core can be significantly reduced down to 0.01 GPa, due to fracturing (Birch, 1966; Goodman, 1989; Schön, 2004; Jeanne et al., 2017). The stiffness of S3DP material is therefore in the range of damaged core material. Changing the printing composites, the printing ratios and further developments in printing techniques (such as altering the grain size distribution, further impregnation with resin or printing under higher compaction) may permit to increase the stiffness of the printed material and adjust it to a desired rock material. Moreover, in certain experiments (King, 1975; Heslot et al., 1994; Scuderi et al., 2016, among others), the desired fault stiffness can be controlled by separate elastic components, so that the stiffness of the rock or surrogate material has minor importance. It is worth pointing out, that in many experiments it is not necessary to reproduce an identical rock stiffness, but to use adequate scaling laws to create surrogate faults (see also Sections 2.4 and 5.3).

2.3 Printing material composition used in this study

Given the important effects of various printing parameters discussed in the previous section, we chose here to vary only two printing parameters, the recoating speed and the binder saturation. The layer orientation and layer thickness remained the same for all specimens. Our cylindrical samples were printed with the printing z axis along the cylinder axis, while the block samples were printed in such a way that the shear interface was aligned with the $x - y$ printing plane (see also Figure 1).

Our S3DP specimens were fabricated using combinations of two recoating speeds, $v_\mathrm{r} = 0.13$ and 0.26 m/s, and two binder contents, $b = 3.8$ and 7.2 wt% of sand (Table 1b). Further material and 3D-printer specifications are given in Table 1a. All four compositions show porosities close to 45%, calculated using the measured sample weight and volume. This porosity is close to the maximum porosity of 48 %, which corresponds to the loosest possible packing of spherical grains with uniform diameter and no binder. Note that we assumed a silica sand density $\rho_\mathrm{s} = 2.65$ g/cm^3 and a binder density $\rho_\mathrm{b} = 1.15$ g/cm^3 (Mitra et al., 2018) for the porosity calculation.

2.4 Analogue fault material

Several applications could be envisaged with the presented technique of 3D-printing with sand. Here we focus on the possibility of designing surrogate experiments in the context of fault mechanics. The dynamic behavior of earthquakes is often idealized using the analogue spring-slider system as shown in Figure 2a (Rabinowicz, 1951, 1956, 1958; Dieterich, 1979; C. Scholz, 2002; Kanamori & Brodsky, 2004). Here the frictional interface between the block and the ground represents the fault zone, which is loaded with an effective normal force F'_{n}. The block is pulled with a slow, constant velocity, v_{∞}, through an elastic spring of stiffness k, which progressively accumulates elastic energy, in a similar way as the rocks surrounding the fault zone do. The frictional behavior can be expressed either by adopting a slip-weakening friction law (Figure 2b) or a rate-and-state one (Figure 2c), or even more advanced frictional models (e.g. Reches & Lockner, 2010; Sammis et al., 2011; Rice et al., 2014; Viesca & Garagash, 2015; Rice, 2017; Rattez et al., 2018a; Collins-Craft et al., 2020, among others).

In the case of the slip-weakening frictional behavior see Figure 2b Palmer and Rice (1973); Andrews (1976); C. Scholz (2002); Di Toro et al. (2011); Stefanou (2019)), the spring-slider analogue system is considered (Lyapunov) unstable, if the spring stiffness k is lower than the critical stiffness of the interfaces $k_{\mathrm{c}}^{\mathrm{sw}} = \Delta\mu \cdot F'_{\mathrm{n}} \,/\, d_{\mathrm{c}}^{\mathrm{sw}}$, where $\Delta\mu \cdot F'_{\mathrm{n}}$ is the frictional drop (corresponding to the static stress change of an earthquake) and $d_{\mathrm{c}}^{\mathrm{sw}}$ is the characteristic slip-weakening distance (Dieterich, 1979; C. Scholz, 2002; Kanamori & Brodsky, 2004; Di Toro et al., 2011; Stefanou, 2019).

On the other hand, when a rate-and-state friction law (Dieterich, 1981a; Ruina, 1983) is employed, the system is (Lyapunov) unstable if the stiffness of the equivalent spring k is lower than $k_{\mathrm{c}}^{\mathrm{rs}} = (b-a) \cdot F'_{\mathrm{n}} \,/\, d_{\mathrm{c}}^{\mathrm{rs}}$ (necessary and sufficient condition for quasi-static motion), where a and b are empirical parameters, which can be obtained as indicated in Figure 2c. In this frictional law, $d_{\mathrm{c}}^{\mathrm{rs}}$ is the characteristic rate-and-state distance (Dieterich, 1981a; Ruina, 1983; Marone, 1998; Scholz, 1998).

In this study, printing interfaces with desired (macro-) roughness allows a direct control of the apparent slip-weakening properties of the interfaces (i.e. of the post-peak frictional response, characterized through $\Delta\mu$ and $d_{\mathrm{c}}^{\mathrm{sw}}$). This property is then exploited for the design of analogue experiments in the laboratory by controlling the post-peak frictional response. Earthquake-like instabilities can then be reproduced in the laboratory by adding a separate elastic component (e.g a spring) of desired stiffness (see Figure 2a, King, 1975; Heslot et al., 1994; Scuderi et al., 2016, among others).

3 Sand-based 3D-printed material characterization

To characterize the basic mechanical and frictional properties of the S3DP material, we carried out: a) unconfined compression tests on cylindrical S3DP specimens and b) shear tests on flat S3DP interfaces. The four different material compositions (Table 1b) were tested in order to analyze the effect of binder content and recoating speed on the mechanical parameters and to choose the most suitable composition for analogue faults.

3.1 Unconfined compression tests

For the unconfined compression test, we used a uniaxial compression frame, which is equipped with a 20 kN loadcell mounted on a servo-mechanical piston. The loading for the following experiments was carried out under displacement control with a rate of 0.1 mm/min, measured by an integrated encoder. The vertical displacement of the top of the specimen was recorded by an LVDT. Cylindrical specimens were printed with 20 mm diameter and 40 mm height. The cylinder axis was aligned with the printing direction z (Figure 1a). For the S3DP material, the weakness planes were aligned with the

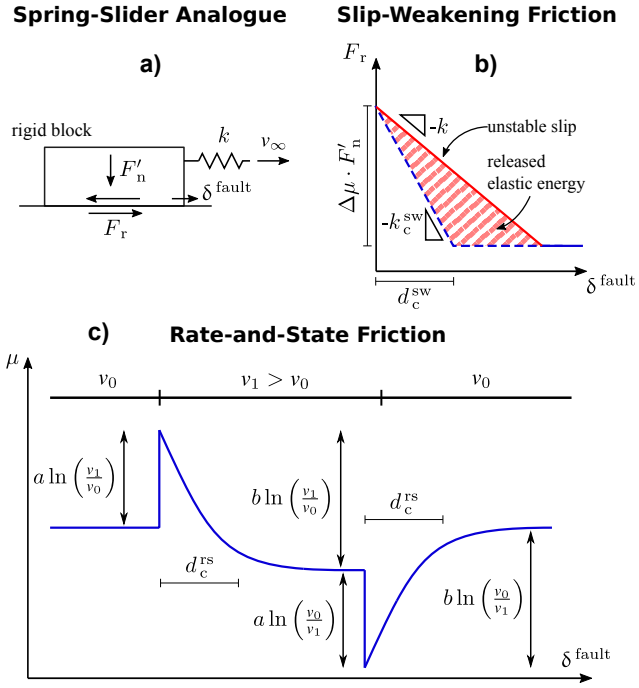

Figure 2. a) Schematic representation of the spring-slider dynamic system, consisting of a rigid block under a constant effective normal force F'_n, pulled with a slow velocity v_∞ through an elastic spring of stiffness k. b) Slip-weakening friction (cf. Palmer & Rice, 1973; Andrews, 1976; Dieterich, 1979; C. Scholz, 2002; Di Toro et al., 2011; Stefanou, 2019): Frictional force F_r over block displacement δ^{fault}. The system is unstable when $k < k_c^{sw} = \Delta\mu \cdot F'_n / d_c^{sw}$, where $\Delta\mu \cdot F'_n$ is the frictional drop due to slip-weakening and d_c^{sw} the characteristic slip-weakening distance. c) Rate-and-state friction (Dieterich, 1981a; Ruina, 1983): Coefficient of friction μ over block displacement δ^{fault}. The system is unstable when $k < k_c^{rs} = (b - a) \cdot F'_n / d_c^{rs}$, where a and b are empirical parameters and d_c^{rs} is the characteristic rate-and-state distance.

printing plane (Gomez, 2017; Gomez et al., 2019). The printing deposition leads to a transversely isotropic material which, to some extent, could mimic the natural, geological deposition mechanism.

For our direct shear specimens, shearing was carried out along this weakness plane. Notice that the layer orientation could influence the shear failure behavior of the S3DP matrix. In particular, this could influence wear, gouge production and the failure of asperities along the printed interfaces (see also Section 5.2). As far as it concerns the bulk properties of the S3DP material, a comprehensive characterization of its anisotropy would require further compression tests, loaded parallel and inclined with respect to the printing layer (cf. Gomez, 2017; Gomez et al., 2019). In this study however, the aim of the compression tests was to get a first qualitative idea of the mechanical properties of the bulk material.

Typical stress-strain curves of the performed UCS tests are presented in Figure 3. More specifically, we are interested in the unconfined compressive strength (UCS), the Young modulus and the post-peak behavior (ductility/brittleness). Good repeatability was reported for tests of the same material composition.

In all of our experiments, we can observe a linear loading path above an axial stress of $\sigma_1 \approx 5$ MPa, leading to a relatively brittle failure. Below that stress level, the slope

of the stress-strain curve is much smaller, indicating a possible plastic compaction due to crack and/or pore closure. After failure, we detect a significant, but gradual softening in the post-peak regime, which can be beneficial in some applications (ductility). Notice that the initial loading section of composition R1 at $\sigma_1 \approx 2$ MPa shows a distinctive plateau, which could also be due to initial misalignment of the specimen or initial local compaction of asperities at the top and bottom end surfaces.

We note that compositions R1 and R3 (low recoating speed) behave similarly, with peak stresses close to 18 MPa. Likewise, compositions R2 and R4 (high recoating speed) show similar responses, but with lower peak strengths, i.e. at around 12 MPa. R2 and R4 specimens showed a more ductile behavior than the others (i.e. shallower and longer strain softening branch). The UCS values are summarized in Figure 4a, showing the increase of strength with lower recoating speed. Slower recoating induces higher packing density, which seems to favor mechanical strength. The binder content has negligible influence on the compressive strength.

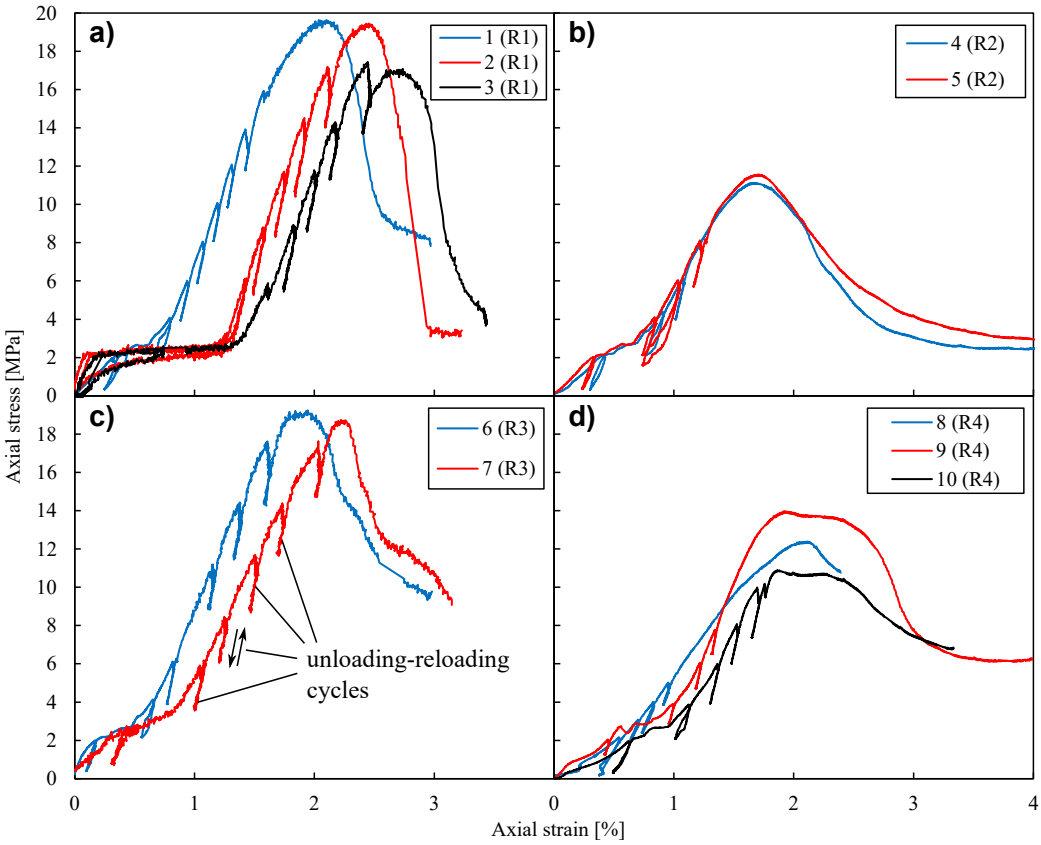

Figure 3. Experimental stress-strain behavior obtained from uniaxial compression tests on specimens with different compositions (Table 1b). The specimens were loaded with a constant displacement rate of 0.1 mm/min. We carried out subsequent unloading-reloading cycles before reaching the peak stress, by unloading each time for about 1.2 to 2.0 MPa, in order to determine the Young modulus from elastic deformations. Strain softening is observed after the peak.

During the loading paths, unloading-reloading cycles were carried out to measure the elastic Young modulus E. This parameter was evaluated through linear regression on the stress-strain curve of each cycle. In Figure 4b, we plot the Young modulus with respect to the vertical stress at the beginning of the respective cycle. We can observe

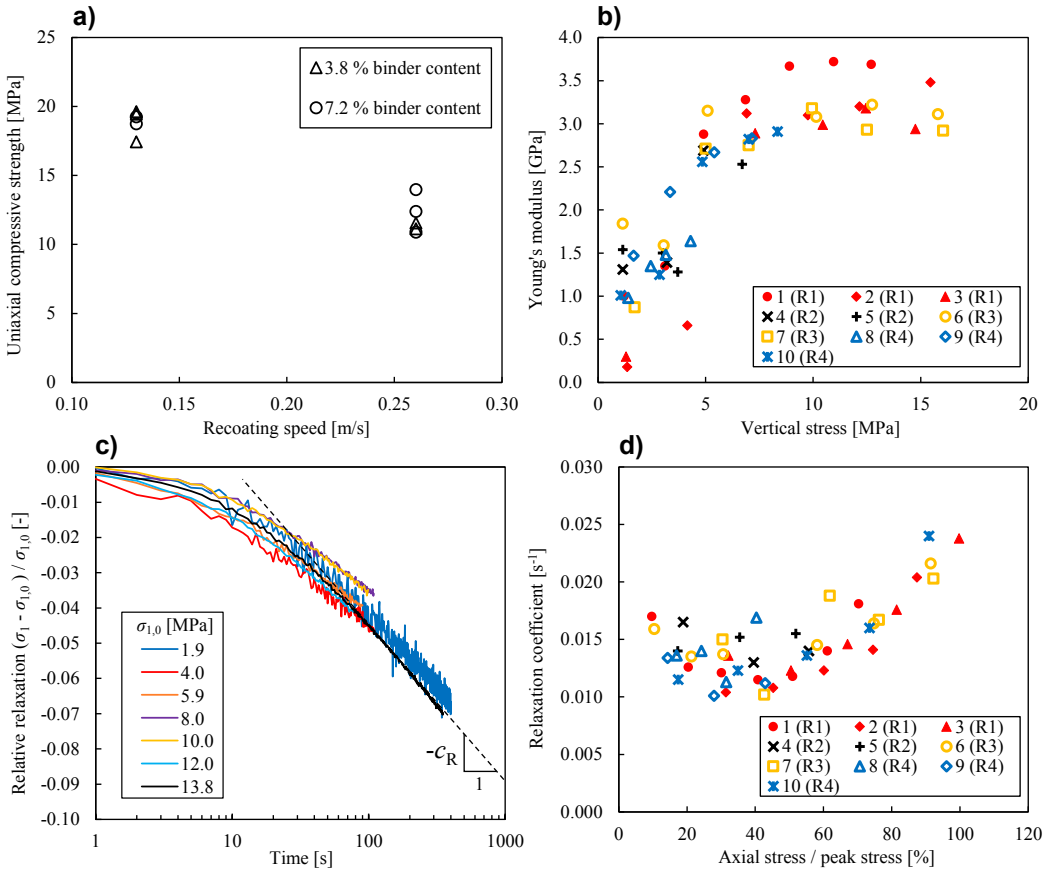

Figure 4. Data taken from the unconfined compression tests 1 - 10 in Figure 3: a) Influence of the recoating speed on the unconfined compressive strength. Different binder contents (Table 1b) have no significant effect. b) Young's modulus evaluated at unloading-reloading cycles at different axial stress levels. c) Relaxation coefficient c_R evaluated at constant displacement stages and under different stress levels. The indicated slope provides an estimation of the relaxation coefficient c_R. d) Relative relaxation with respect to time under various initial axial stress levels $\sigma_{1,0}$.

that E varies from around 0.2 up to 3.7 GPa. While the composition of the specimens does not notably affect the Young modulus E, the vertical stress has a significant impact on the stiffness. Even though we detect a rather large dispersion of values, we can observe an increase of the Young modulus with vertical stress. At $\sigma_1 = 2$ MPa, we measured $E \approx 1.0$ GPa, which increases up to $E \approx 3.3$ GPa at $\sigma_1 = 6$ MPa. For higher stresses, the Young modulus remains practically constant.

Before each unloading-reloading cycle, the displacement was stopped for a certain time, which allowed us to measure the vertical stress relaxation. The decrease of vertical stress, starting from the initial value $\Delta\sigma_1 = \sigma_1 - \sigma_{1,0}$, was analyzed relative to the initial stress $\sigma_{1,0}$, giving the dimensionless relative relaxation. Figure 4c shows a typical result of the relative relaxation with respect to time, measured on different stages for specimen 1 (composition R1). After a time of 30 s, we observe a linear behavior with respect to log-time. The relaxation coefficient c_R can be evaluated from the slope of the curve and its values are presented in Figure 4d in function of the normalized vertical stress (initial vertical stress over compressive strength). Independently of the sample compo-

sition, we find values of c_{R} varying between 0.010 and 0.017 s^{-1} at a vertical stress below 80 % of the compressive strength, while above that stress level, c_{R} increases up to 0.024 s^{-1} at 100 % compressive strength.

In terms of compressive strength, we found a range of values between 10 and 20 MPa, similar to the values obtained by Gomez et al. (2019) on a similar material. The observed values for compressive strength and Young's modulus are comparable to those of weak sandstones (porosity of approximately 25 %, Dobereiner & Freitas, 1986; Papamichos et al., 2000). Interestingly, we can observe an evolution of Young's modulus with vertical stress, such as in natural sandstones (e.g. Pimienta et al., 2015). This behavior is often explained through the closure of micro-cracks, which increases the grain-to-grain contact area and consequently the stiffness.

Note that the Young modulus, the peak strength and the relaxation characteristics were determined in this study always for a loading direction perpendicular to the printing layer. For loading parallel to the layer, one can expect different properties due to the anisotropic micro-structure of the material, but this exceeds the scope of the current work. For instance, Gomez (2017) showed for a similar S3DP material, that under loading parallel to the printing layer with respect to perpendicular loading, the strength decreased from 17.1 to 14.4 MPa, the failure characteristics changed from ductile to brittle and the Poisson ratio increased from 0.19 to 0.25, while the Young modulus remained at 1.7 GPa.

3.2 Direct shear experiments on flat interfaces

For direct shear experiments, we used the direct shear device shown in Figure 5a, which is designed for specimens composed of two blocks. The bottom one has dimensions equal to 140x100x10 mm^3 and the top one equal to 100x100x25 mm^3 (length x width x height). These blocks were printed with their height axis perpendicular to the printing layer.

The length of the bottom block is higher than the one of the top block, in order to assure constant contact area (100x100 mm^2) during shearing. In the vertical direction, the controlled normal force F_{n} results in a normal stress σ_{n}, which is quasi-uniform over the interface (Tzortzopoulos et al., 2019). The vertical displacement was measured by an integrated LVDT. In the horizontal direction, a ram permits to move the lower part of the device. We performed displacement controlled (δ) experiments. The horizontal displacement induces a shear stress τ_{n}, which is considered to be uniformly distributed over the interface. During shearing, loose material might detach from the blocks. However, the sheared interface is 100 mm wide, prohibiting grain removal from the shear interface (plane-strain conditions). Moreover, the loading frame prevents loss of grains from the lateral sides of the specimen.

For each material composition R1 - R4, we tested two specimens under a normal stress of 500 kPa and a shear displacement rate of 0.5 mm/min. Two additional specimens of composition R1 were sheared under 100 kPa normal stress. The apparent friction coefficient, presented for some typical results in Figure 5b, reached a constant residual plateau for the investigated shear displacement up to 6 mm. The initial load-displacement branch includes elastic deformation, but also compression and sliding due to alignment of the sample blocks with the loading frame. Moreover, gouge is formed, which then undergoes steady-state shearing. Steady-state or critical-state shearing (Roscoe et al., 1958; Wood, 1991) is accompanied by gouge production due to grain detachment. Between the two phases a smooth transition is observed. The average values of this residual friction coefficient under 500 kPa normal stress are 0.58 for R1, 0.60 for R2 and 0.63 for R3 and R4. Decreasing the normal stress in tests on composition R1 did not change the apparent friction coefficient, confirming Coulomb's assumption of proportionality. The experiments showed good repeatability.

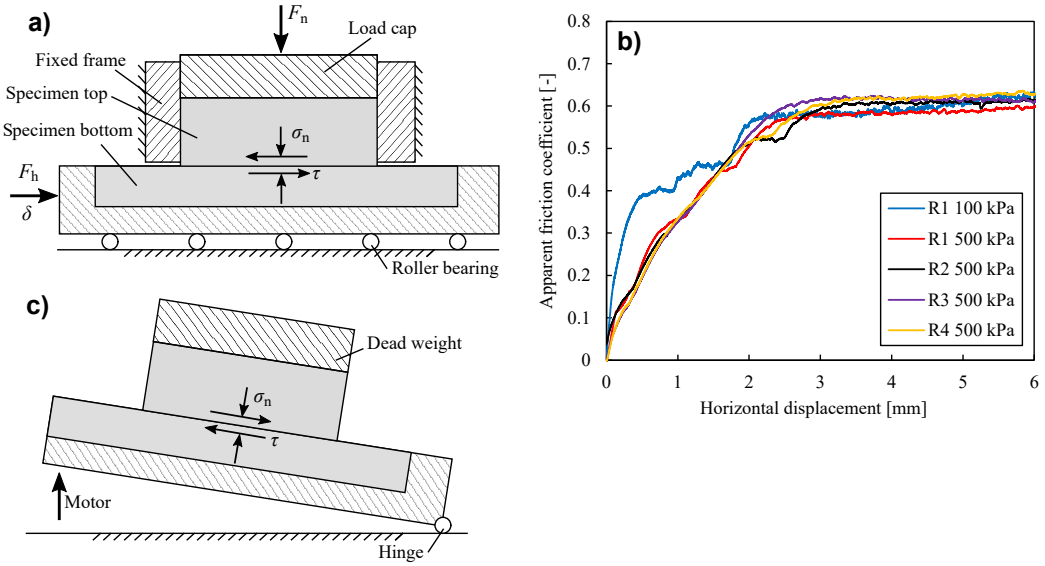

Figure 5. a) Schematic plan of the direct shear apparatus. The normal force F_n and the horizontal displacement δ are controlled. b) Evolution of the apparent friction coefficient shown on one representative result for each material composition and normal stress level. c) Configuration of the inclined plane shear test.

The measurements from the direct shear tests were verified through additional friction tests on composition R1, using an inclined plane configuration (Figure 5c). In these verification tests, specimens consisting of lower and upper blocks with flat interfaces (equivalent dimensions as the specimens used for direct shear tests), were placed on a horizontal metal plate. The lower block was prevented from sliding on the plate, while the upper block was unconstrained. An additional weight of 1.0 kg was placed on top of the upper block. The plate was slowly inclined, until the upper block started to slide. By measuring the inclination angle, the friction coefficient of the interface could be determined. We carried out four tests in this way, showing an average friction coefficient $\mu = 0.62$ (corresponding to a friction angle of 31.8°) with a standard deviation of 5.0 %. This friction coefficient is close to the value of 0.58 obtained on the R1 composition using the direct shear apparatus, which confirms the results of the more complex device. Zero cohesion was measured in all the tests.

Proceeding one step further with the characterization of the flat interfaces, we carried out velocity stepping experiments under constant normal load, in order to estimate the rate-and-state parameters a, b and d_c^{rs} (see Figure 2c). The same direct-shear apparatus and testing configuration were used as in Figure 5a. We performed two tests using specimens made of R2 composition under 500 kPa of normal stress. Initially, the specimens were loaded for 5 mm with a constant shear displacement rate of $v_0 = 5\,\mu$m/s in order to assure steady-state sliding of the mobilized block. An abrupt decrease of the velocity by one order of magnitude to $v_1 = 0.5\,\mu$m/s followed. This velocity was kept constant for a total displacement of 2 mm, until the velocity increased again instantly to v_0. After 2 mm of sliding, a last abrupt velocity reduction to v_1 took place. The response of the specimens under these velocity steps can be observed in Figure 6.

More specifically, in Figure 6a, the time-history of the horizontal displacement is displayed, where the velocity steps, interchangeably between v_0 and v_1, are easily distinguishable. In Figure 6b, the apparent friction coefficient in terms of the horizontal displacement is plotted, along with a closer look to the frictional response due to an abrupt

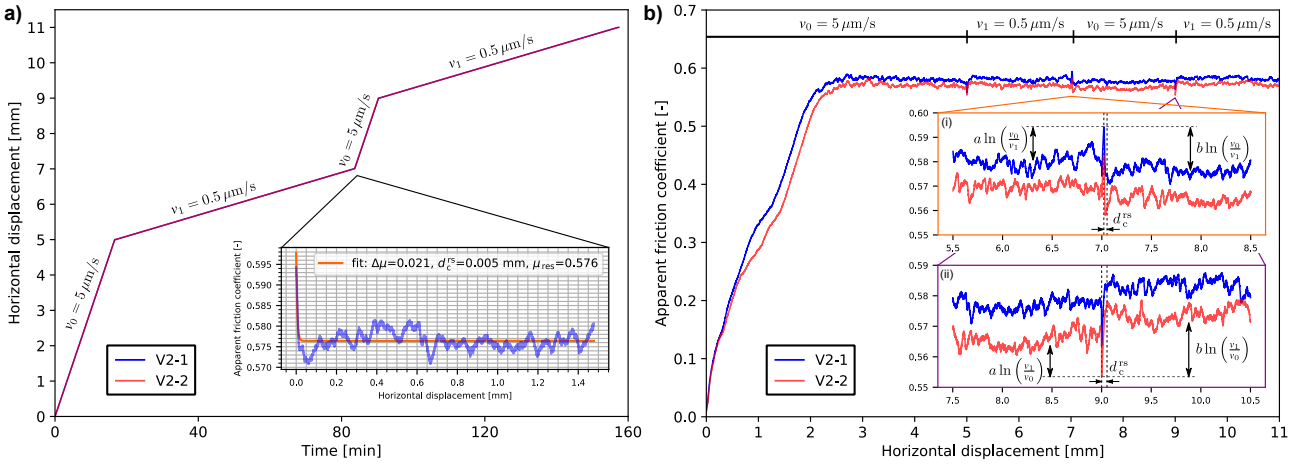

Figure 6. a) Horizontal displacement over time. The different applied displacement-rates are also illustrated indicating their duration. The inset shows an example of an exponential fitting which is employed for calculating d_c^{rs} for each velocity step. b) Apparent friction coefficient with respect to the horizontal displacement of the moving block. In the insets (i) and (ii), a closer look to an increase and decrease of velocity is presented, respectively.

(i) increase (orange framed inset) and (ii) decrease (purple framed inset) of block's velocity. In the case of a velocity increase (inset (i)), an instant frictional strengthening is observed of $\Delta\mu = a\ln(v_0/v_1)$ (from the steady-state). Then an exponential decay of the friction occurs leading to the next frictional steady-state value due to the faster velocity v_0. The exact opposite happens for a velocity decrease as indicated in the inset (ii). The difference between the steady-state values before and after each velocity step is denoted as $\Delta\mu_{ss}$ and is equal to $(a-b)\ln(v_0/v_1)$. The distance that it takes for the friction to reach its new steady-state after a velocity change is noted as d_c^{rs}.

The parameters $a-b$ and d_c^{rs} are involved in the study of the stability of the analogue spring-slider model under the rate-and-state friction (see Section 2.4 and Figure 2c). By taking into account the average steady-state friction before and after each velocity step and considering an order of magnitude increase of velocity, the average difference $(a-b)_{in}$ is equal to -0.0019, while for an equivalent decrease of velocity is $(a-b)_{dcr} = -0.0037$. For estimating the characteristic rate-and-state distance d_c^{rs}, we performed an exponential fitting to the frictional decay raw data utilizing the least-squares method, as it is illustrated in the inset of Figure 6a (Rice & Ruina, 1983; Gu et al., 1984; Bhattacharya et al., 2015). Consequently, the characteristic distance for the rate-and-state friction law following a factor of 10 rise of the velocity is $d_{c,in}^{rs} = 0.005$ mm, while for an equivalent drop is $d_{c,dcr}^{rs} = 0.014$ mm.

These results show that for relatively slow velocities and only if the sliding block has reached its steady-state, the S3DP material displays a rate-and-state dependency (Dieterich, 1981a; Dieterich & Kilgore, 1994; Hunfeld et al., 2019). Therefore, considering the micro-behavior of this 3D-printed material, these experiments give birth to an additional small length-scale of the order of approximately $0.1D_{50}$. However, this rate-and-state behavior plays a secondary role in the design of interfaces with custom (slip-weakening) frictional properties. As shown in the next Sections, this is due to the possibility of adjusting the macro-roughness using 3D-printing.

4 Design of interfaces with controlled friction

Once the basic mechanical properties of the sand printed material are identified, it is possible to design the geometry of the printed interfaces, in order to give them the desired frictional properties. These properties include the peak friction, the residual friction, and the characteristic slip-weakening distance. Moreover, we can control the exact evolution of friction with slip, giving us important flexibility in experiments.

4.1 Joint friction model

Modeling the frictional behavior allows us to better understand the underlying physical mechanisms and enables us a to design interfaces of desired frictional properties. According to Newland and Allely (1957); Patton (1966), and assuming Coulomb friction, the friction coefficient of rock joints is:

$$\mu = \frac{\tau}{\sigma_{\mathrm{n}}} = \tan(\phi_{\mathrm{b}} + i) \tag{1}$$

where ϕ_{b} is called basic friction angle and i effective roughness, or i-value in the case of rock joints (Barton, 1973). The effective roughness is the inclination of asperities along the interface.

According to Barton (1973), the value of ϕ_{b} corresponds to the residual friction angle, measured on saturated, planar rough-sawn or sand-blasted surfaces of the rock. This author has summarized literature data for sand-blasted and sawn surfaces, showing that most rocks have basic friction angles of approximately between 25° and 35°. The measured basic friction of the sand-based 3D printed material was found in the same range (around 30°, see Section 3.2), which makes it a good candidate for a rock analogue, as far as it concerns frictional properties.

By appropriately designing i in terms of slip, one can control the evolution of the apparent friction coefficient μ. In this way it is possible to imitate a great variate of frictional behavior in experiments. In order to demonstrate this idea, we apply Patton's friction relation (Eq. (1)) for periodic sine-wave asperities. This roughness profile is expressed as a function of the shear displacement δ, defined by an amplitude A_0 and a wavelength λ. In Figure 7, we present the geometry of the sinusoidal asperities. According to Eq. (1), the maximum friction is expected at the maximum profile angle i, where we set $\delta_{\mathrm{pp}} = 0$. The profile height, h_{p}, can be expressed as a function of the shear displacement δ_{pp}, resulting in $h_{\mathrm{p}}(\delta_{\mathrm{pp}}) = A_0 \sin(2\delta_{\mathrm{pp}}\pi/\lambda)$. The asperity inclination gives us the asperity friction coefficient μ_{A}, obtained through differentiation of h_{p} with respect to δ_{pp}:

$$\mu_{\mathrm{A}}(\delta_{\mathrm{pp}}) = \tan\left[i(\delta_{\mathrm{pp}})\right] = \frac{\mathrm{d}h_p(\delta_{\mathrm{pp}})}{\mathrm{d}\delta_{\mathrm{pp}}} = 2\pi\frac{A_0}{\lambda}\cos\left(2\pi\frac{\delta_{\mathrm{pp}}}{\lambda}\right) \tag{2}$$

where the maximum and minimum asperity friction μ_{A} are given by $\pm 2\pi A_0/\lambda$. Inserting Eq. (2) in (1), one can calculate the total apparent friction coefficient:

$$\mu(\delta_{\mathrm{pp}}) = \frac{\mu_{\mathrm{b}} + \mu_{\mathrm{A}}(\delta_{\mathrm{pp}})}{1 - \mu_{\mathrm{b}}\mu_{\mathrm{A}}(\delta_{\mathrm{pp}})} \tag{3}$$

where $\mu_{\mathrm{b}} = \tan\phi_{\mathrm{b}}$ is the basic friction coefficient (see Section 4.3).

In addition, the oscillating vertical compaction-dilation $\delta_{\mathrm{v,A}}$ due to the sliding over asperities (Figure 7) can be derived from the profile height $h_{\mathrm{p}}(\delta_{\mathrm{pp}}) = A_0 \sin(2\pi\delta_{\mathrm{pp}}/\lambda)$. Therefore, dilatancy can be designed as well, which, for the sinusoidal asperities, is equal to:

$$\delta_{\mathrm{v,A}}(\delta_{\mathrm{pp}}) = A_0\left[1 + \sin\left(2\pi\frac{\delta_{\mathrm{pp}}}{\lambda}\right)\right] \tag{4}$$

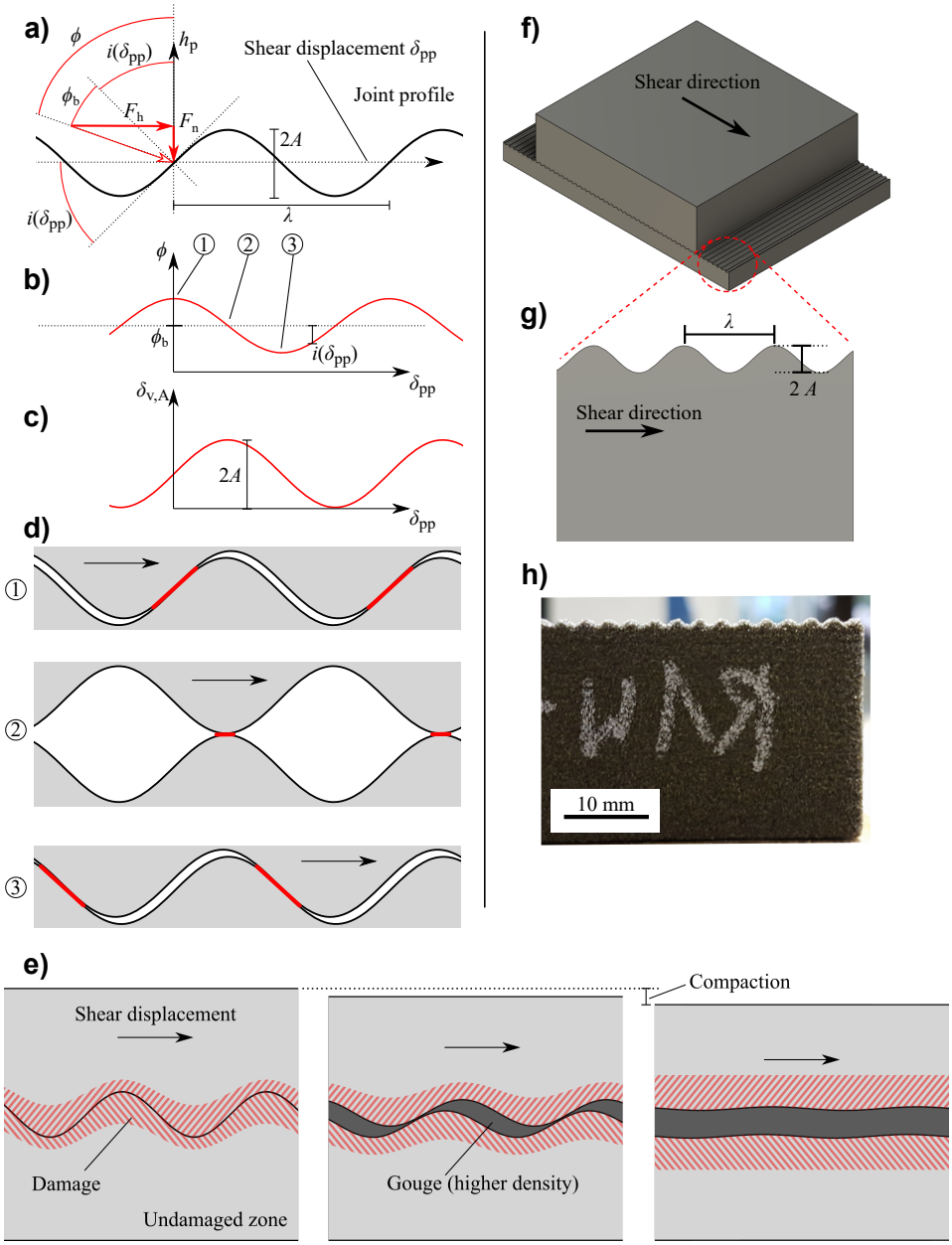

Figure 7. Friction model for a joint with periodic asperity geometry, illustrated using a sine-wave profile. a) Force diagram on the position $\delta_{pp} = 0$, where the asperity inclination i is the highest. The apparent total friction angle, which gives the relationship between F_h and F_n, is the sum of i and ϕ_b. b) Oscillation of the total friction angle ϕ around the basic friction angle ϕ_b with amplitude i, depending on the shear displacement. c) Vertical displacement of the top interface. d) Asperity contact orientation (red in online version), which changes with progressing displacement and affects the total friction. Wear and compaction is neglected in this schema, so that the interface geometry remains unchanged ($A = A_0$). e) Schematic representation of gradual wear of asperities. Abraded grains form a gouge layer between the interfaces. Total compaction can be due to the compaction in the damage zone and in the gouge layer. f) 3D model for printing the two direct shear specimen blocks with wave interfaces. g) Cross-section and zoom on the sine-wave interface with amplitude $A = 0.42$ mm and wavelength $\lambda = 2.80$ mm. h) Image of a printed specimen, zoomed on the interface.

Notice that this relation is purely geometrical and kinematic and neglects any deformations due to high normal stress and/or hertzian contacts. These two factors could be taken into account in a more detailed analysis.

4.2 Wear and gouge formation

In our friction model, we intend to take into account the wear of asperities and the formation of gouge, due to the detachment of grains from the S3DP matrix (Figure 7e). Note that this gouge formation could mimic the creation of gouges in real faults (Marone & Scholz, 1989; Marone et al., 1990; Rattez et al., 2018a, 2018b).

Queener et al. (1965) proposed a general law for wear, composed of an exponential transient and a linear steady-state wear, which is compatible with wear observations in rock joint shear experiments (Power et al., 1988).

Abrasion gradually reduces the asperity amplitude (Li et al., 2016) (Figure 7e) and therefore the asperity friction affected by wear is denoted by $\mu^*_{\mathrm{A}}(\delta_{\mathrm{pp}})$. For very large displacements, $\mu_{\mathrm{A}}(\delta_{\mathrm{pp}})$ becomes zero and $\mu = \mu_{\mathrm{b}}$ (Eq. (3)). We consider here exponential abrasion, which reduces the apparent asperity friction coefficient $\mu^*_{\mathrm{A}}(\delta_{\mathrm{pp}})$:

$$\mu(\delta_{\mathrm{pp}}) = \frac{\mu_b + \mu^*_{\mathrm{A}}(\delta_{\mathrm{pp}})}{1 - \mu_{\mathrm{b}}\mu^*_{\mathrm{A}}(\delta_{\mathrm{pp}})} \tag{5}$$

$$\mu^*_{\mathrm{A}}(\delta_{\mathrm{pp}}) = \mu_{\mathrm{A}}(\delta_{\mathrm{pp}})\, e^{-c_{\mathrm{w}}\delta_{\mathrm{pp}}} \tag{6}$$

The frictional behavior of this designed interface can therefore be adjusted through two asperity properties and two material parameters. These parameters are the wavelength λ, which governs the period in which the friction oscillates, and the amplitude A_0, which defines the asperity friction. Moreover, the material composition affects the basic friction μ_{b} and the wear coefficient c_{w}.

In terms of vertical displacement, the maximum compaction $\delta_{\mathrm{v,max}}(\delta)$ is a function of the total shear displacement δ and can be described by an empirical exponential law (Power et al., 1988):

$$\delta_{\mathrm{v,max}}(\delta) = \delta_{\mathrm{v},\infty}\left(1 - e^{-c_{\mathrm{v}}\delta}\right) \tag{7}$$

where c_{v} is the vertical compaction coefficient and $\delta_{\mathrm{v},\infty}$ the final steady state compaction.

Moreover, we can superpose the oscillating vertical compaction-dilation $\delta_{\mathrm{v,A}}$ due to the sliding over asperities (Eq. (4), see also Figure 7) to Eq. (7). As described above (Eq. (6)), the amplitude of the asperities decreases due to wear, governed by the wear coefficient c_{w}. The asperity dilation accounting for wear is then written as:

$$\delta^*_{\mathrm{v,A}}(\delta_{\mathrm{pp}}) = A_0\, e^{(-c_{\mathrm{w}}\delta_{\mathrm{pp}})}\left[1 + \sin\left(\delta_{\mathrm{pp}}\frac{2\pi}{\lambda}\right)\right] \tag{8}$$

The total vertical displacement is the sum of compaction and asperity dilation:

$$\delta_{\mathrm{v}}(\delta_{\mathrm{pp}}) = \delta_{\mathrm{v,max}}(\delta) + \delta^*_{\mathrm{v,A}}(\delta_{\mathrm{pp}})\,, \quad \delta = \delta_{\mathrm{pp}} + \delta_1 \tag{9}$$

where δ_1 is the total shear displacement at the first peak of the apparent friction coefficient. Power et al. (1988) stated that in laboratory shear tests, most of the wear occurs in the "transient wear phase". Laboratory specimens have a finite roughness scale,

and most of that initial roughness is destroyed during the initial, transient wear phase. Moreover, created gouge material often isolates the bare rock interfaces and reduces the apparent friction (Figure 7e). According to these authors, this first transient wear is followed by steady-state wear, which continues in laboratory tests under a relatively slow rate, as most of the asperities are flattened out. In real faults however, fault roughness is self-affine and covers a much larger range of scales (e.g. Schmittbuhl et al., 1993; Candela et al., 2012). As a result, the size of the asperities that must be broken increases approximately linearly with displacement. Hence, real faults never reach a steady state wear as experimental faults do (Power et al., 1988). However, similar to our experimental results, the recent work of Dascher-Cousineau et al. (2018), using numerous samples from fault outcrops, showed that at a small scale (< 10 mm) fault surfaces indeed smoothen with slip. Note that in our experiments, we investigate a finite roughness scale, equal to the size of the sine-waves. Steady state wear is therefore expected to be negligible and not considered in the model.

4.3 Direct shear experiments with designed roughness

Direct shear experiments were performed on S3DP material with controlled roughness properties, to study the effectiveness of our theoretical friction design approach. For this purpose, we printed sine-wave interface asperities with a constant amplitude $A = 3D_{50} = 0.42$ mm and constant wavelength $\lambda = 20D_{50} = 2.80$ mm, as shown in Figure 7f-h.

A series of direct shear tests under a constant normal stress of 500 kPa was carried out on samples of the four different compositions. The specimens were initially loaded with a normal stress of 500 kPa and sheared under constant normal stress and constant displacement rate of 0.5 mm/min for 10 mm. After the maximum displacement was reached, the specimen was sheared in the reverse direction, until its initial position. In this way, a full loading cycle was performed, corresponding to a total of 20 mm of accumulated slip. Figures 8 (compositions R1 and R2) and 9 (compositions R3 and R4) present the evolution of the measured friction coefficient and the vertical displacement with progressing horizontal displacement. In particular, we show the apparent friction coefficient μ, defined as the ratio of $F_{\mathrm{h}}/F_{\mathrm{n}}$. Negative values correspond to reverse shearing. One can clearly observe oscillations in the post-peak regime of the friction behavior, due to the wave geometry of the interfaces. The interlocking printed asperities induce a much higher peak friction, close to 1.0, compared to the one measured on the flat surface, close to 0.6. Once we exceed the peak, the friction decreases and drops to a lower level than the one determined on flat specimens (negative asperity friction angle i, see Eq. (1)). Then, the friction rises and falls in the form of damped oscillations, due to wear. In terms of vertical displacement, the specimens exhibit an overall compaction during shearing, combined with dilation peaks of decreasing amplitude.

In Table 2, we present different frictional properties evaluated from the experimental results (Figures 8 and 9). The maximum friction coefficient measured at the first peak (μ_1) is shown along with the respective block's displacement (δ_1). At the end of the reverse loading (negative apparent friction), the amplitude of friction oscillations becomes almost zero. Inspecting the specimens after the experiments confirmed that wear has flattened out the sine-wave asperities and left an almost flat interface. One can estimate the residual friction coefficient μ_∞ from the mean friction in this part of the experimental curve, which results in being almost identical to μ_{b} (asymptotical approximation for infinite sliding). In theory, differences may arise due to a higher amount of gouge material present when evaluating μ_∞. Comparing the values of μ_∞ with the results from flat interface shear experiments, no significant difference can be observed. The wavelengths λ_1 and λ_2 are the slip distances between two points of maximum and minimum friction, respectively. Their average value is λ, which corresponds in theory to the wavelength of the printed interface. It is important to note, that the characteristic slip-weakening dis-

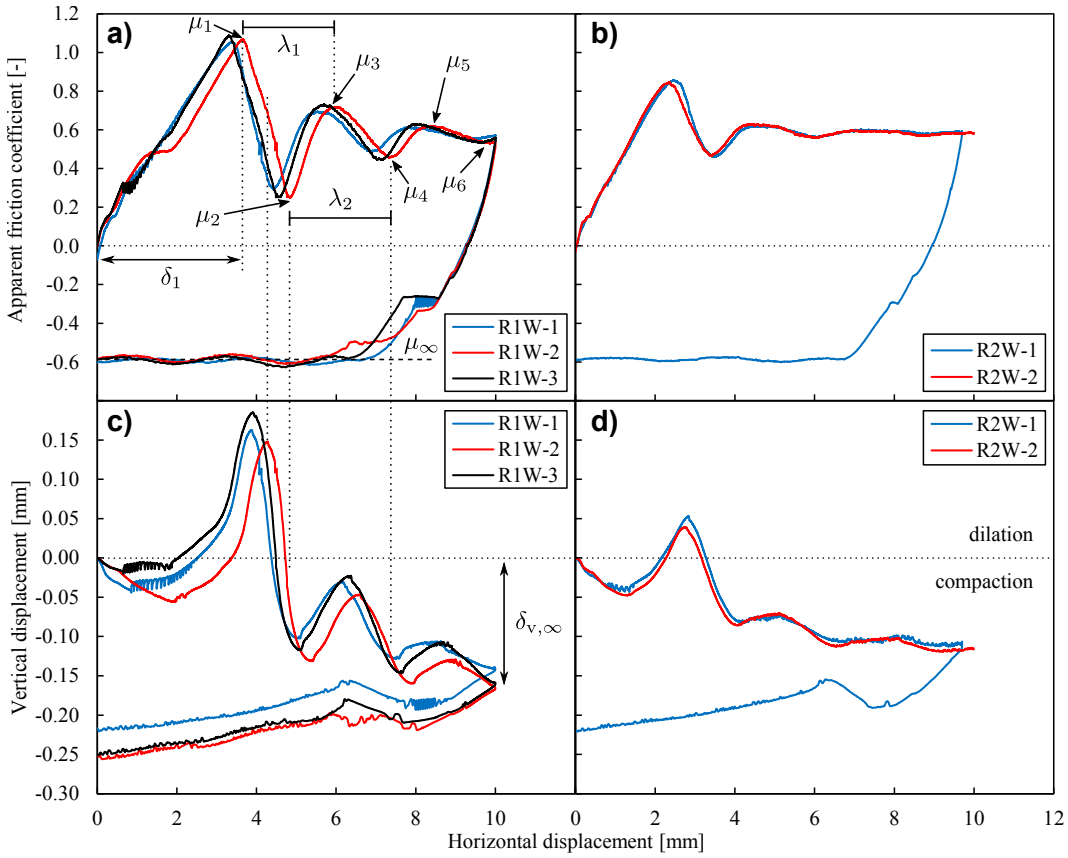

Figure 8. Results of direct shear experiments under 500 kPa normal stress on specimens R1 and R2 (Table 2). a), b) Friction coefficient and c), d) vertical displacement with respect to horizontal shear displacement. Note that due to technical problems, the reverse shearing of R2W-2 was not carried out.

tance d_c^{sw} (Figure 2b), over which the apparent friction decreases from its maximum to its minimum, is here equal to half of the wavelength λ (for sinusoidal interfaces).

4.3.1 Effect of material composition

For high binder content, the recoating speed (packing density) appears to have a minor influence on the friction, as we observe similar values $\mu_1 = 0.96$ and 0.93 for R3 and R4, respectively. For low binder content, we measured $\mu_1 = 1.07$ for R1 and 0.88 for R2. According to our results, higher density induces higher friction. Moreover, for high density, the friction is higher under low binder content. This is probably due to a higher possibility for grains to interlock in the absence of binder. The friction for large shear displacement μ_∞ does not appear to be significantly influenced by the material composition, providing values close to 0.6 (Table 2), which is equal to μ_b measured on flat specimens in Section 3.2.

Regarding the average wavelength λ, we cannot see any clear influence of the material composition. These values are close to the designed geometric wavelength of the interface $\lambda = 2.40$ mm. Note that the vertical displacement shows the same wavelength, but, as expected, here the oscillations are shifted by $\approx \lambda/4$. This evidences that the behavior of vertical displacement is correlated with the asperity profile. In other words, the friction coefficient reaches its local extrema when the inclination of asperities (the

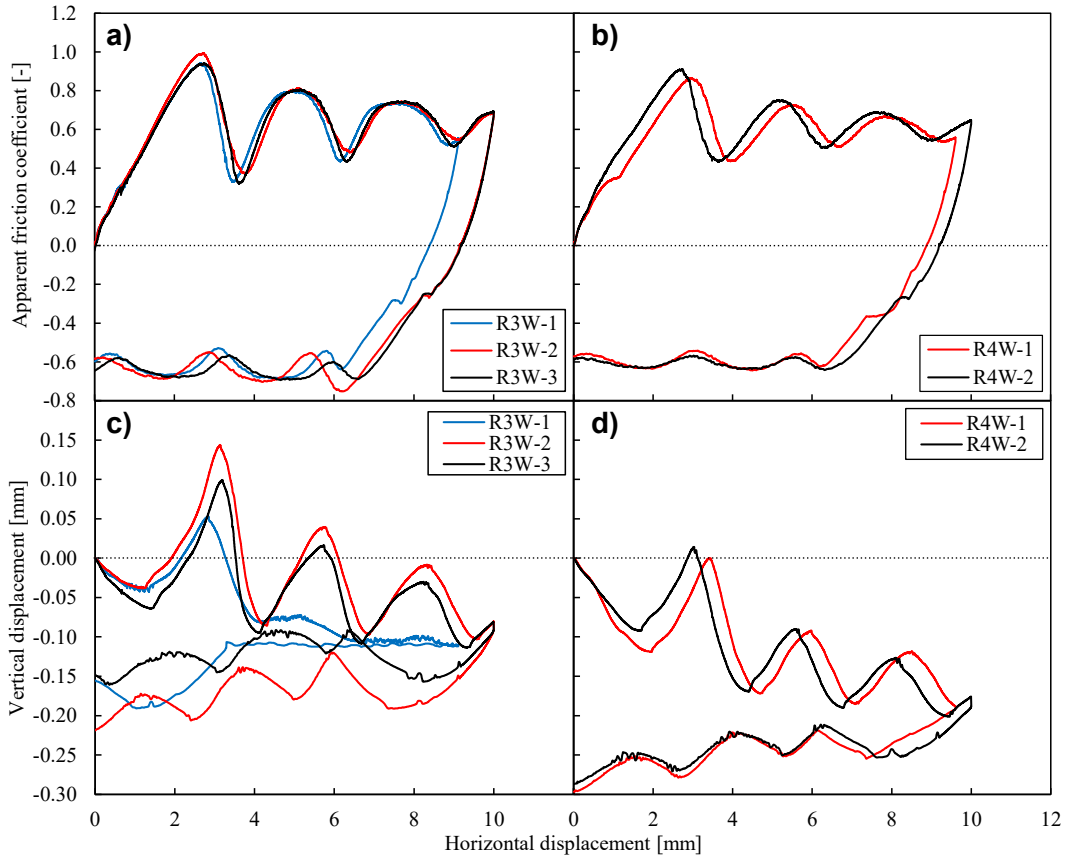

Figure 9. Results of direct shear experiments under 500 kPa normal stress on specimens R3 and R4 (Table 2). a), b) Friction coefficient and c), d) vertical displacement with respect to horizontal shear displacement.

slope of the vertical displacement over horizontal displacement) also has a local extremum (Figures 8 and 9).

The decrease of the friction amplitude differs between the compositions due to wear. For the R1 and R2 specimens (low binder content) the reduction of the amplitude is more prominent (Figure 8), and we observe a nearly constant friction at the end of the first loading phase and during the reverse loading. This residual friction coefficient corresponds to the one of a planar interface, due to complete abrasion of the asperities. This friction reduction can be approximated with an exponential law (Eq. (6)). Rewriting Eqs. (6) and (5), we can determine the relative asperity friction R_{w}, which is initially equal to 1.0 and decreases to zero for progressing wear:

$$R_{\mathrm{w}} = e^{-c_{\mathrm{w}}\delta_{\mathrm{pp}}} = \frac{(|\mu_i - \mu_\infty|)(1+\mu_1\mu_\infty)}{(\mu_1 - \mu_\infty)(1+\mu_i\mu_\infty)} \tag{10}$$

The relative asperity friction is plotted for a typical experiment (R1W-1) in Figure 10a, on which we can obtain the wear coefficient c_{w} through least square fitting (Table 2).

We observe a stronger dependency of the wear characteristics on binder content than on recoating speed. Compositions with a binder content $b = 3.8\%$ show c_{w} between

approximately 0.4 and 0.6, while for $b = 7.2$, we measured c_w between approximately 0.2 and 0.4. Increasing the recoating speed, from 0.13 to 0.26 m/s, the average value of c_w increases for about 0.1.

Table 2. Mean values of the parameters determined from the direct shear tests under $\sigma_n = 100$ and 500 kPa on wave interfaces (see also Figures 8, 9 and 11), and their standard deviation (SD). The amplitude A_0 is back-calculated using Eq. (12).

	σ_n	μ_1		λ		δ_1		μ_∞		c_w		$\delta_{v,\infty}$		c_v		A_0
		mean	SD	mean	SD	mean	SD	mean	SD	mean	SD	mean	SD	mean	SD	
	[kPa]	[-]	[%]	[mm]	[%]	[mm]	[%]	[-]	[%]	[-]	[%]	[-]	[%]	[-]	[%]	[mm]
R1	100	1.03	6.0	2.67	1.6	2.13	6.1	0.50	2.8	0.14	17.1	-0.16	24.7	0.40	2.6	0.149
R1	500	1.07	1.8	2.41	4.4	3.45	5.4	0.57	2.0	0.45	26.0	-0.18	5.6	0.21	8.9	0.118
R2	500	0.85	0.8	2.45	2.0	2.41	2.9	0.58	1.2	0.60	4.7	-0.12	10.5	0.36	29.9	0.071
R3	500	0.96	3.2	2.55	0.8	2.71	2.0	0.61	1.9	0.19	12.7	-0.11	4.6	0.42	21.3	0.091
R4	500	0.89	3.6	2.54	1.1	2.86	5.7	0.60	1.2	0.26	0.8	-0.20	7.1	0.43	29.5	0.078

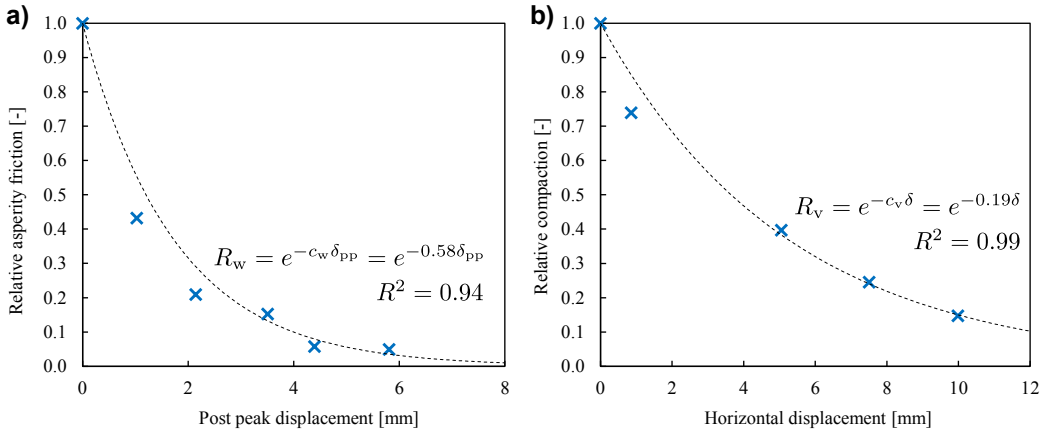

Figure 10. a) Decrease of relative asperity friction with progressing displacement and wear on a typical wave interface shear test (R1W-1). The wear coefficient c_w can be evaluated using an exponential fit. b) Measured relative vertical compaction on a typical wave shear experiment (R1W-1). The compaction is modeled through an exponential law, where the wear coefficient c_v can be evaluated using an exponential fit.

Evaluating the local minima $\delta_{v,i}$ of the vertical displacement evolution δ_v, one observes a general compaction, which starts immediately at $\delta = 0$, before the first friction peak. For large δ, the curves appear to approach a constant vertical displacement $\delta_{v,\infty}$ (cf. critical state, e.g. Wood, 1991). This global compaction is represented by the exponential law (Eq. (7)). Equation (7) can be rewritten, to introduce the relative compaction R_v, which can be evaluated at the local peaks of vertical displacement:

$$R_v = e^{-c_v \delta} = 1 - \frac{\delta_{v,i}}{\delta_{v,\infty}} \tag{11}$$

The relative compaction values, determined on a typical experiment, are presented in Figure 10b. One can obtain the values of c_v and $\delta_{v,\infty}$ by a least square error fit. This

relationship captures only the overall vertical compaction, while in the experiments, we also observe significant oscillations due to asperities. In the following section, we are able to model these peaks of vertical displacement using Eqs. (7) - (9) with previously evaluated properties. Consequently, no additional model parameters are required.

4.3.2 Effect of normal stress

In order to explore the influence of the applied normal stress on shear behavior, we carried out the same shear experiments under 100 kPa normal stress on specimens made of composition R1 (Figure 11, Table 2). The most important difference between the cases of 100 kPa and 500 kPa is observed on the wear, presented in terms of the wear coefficient c_{w} in Figure 11c. Otherwise, Coulomb's assumption of proportionality is valid. By reducing the normal stress, the decay of the friction oscillation is strongly reduced, giving a lower wear coefficient. Due to the lower normal stress, local stresses at the asperities decrease, resulting in less breakage/chipping of the asperities. This becomes also clear on the measured specimen weight after the tests, which was almost two times higher for test under 500 kPa normal stress (average loss of ~ 1.7 g under 100 kPa and ~ 3.2 g under 500 kPa).

No effect of the normal stress on the first peak friction coefficient μ_1 was reported (Figure 11d). Conversely, the residual friction μ_∞ appears to be slightly influenced by the normal stress (Figure 11e). Higher normal stress (500 kPa) leads to higher friction ($\mu_\infty \approx 0.57$), while under 100 kPa, we recorded $\mu_\infty \approx 0.50$.

4.4 Validation of the design model

We use the parameters evaluated on the five different test configurations (four compositions, one additional normal stress level) and insert them in the model equations for calculating the apparent friction coefficient μ (Eq. (5)) and the vertical displacement δ_{v} (Eq. (9)) in function of the shear displacement δ. The effective amplitude A_0 is determined indirectly from the wavelength, the basic friction and the first peak friction coefficient $\mu = \mu_1$ (Eqs. (2) and (3)):

$$A_0 = \frac{\lambda(\mu_1 - \mu_{\mathrm{b}})}{2\pi(1 + \mu_1\mu_{\mathrm{b}})} \tag{12}$$

This model parameter A_0 can differ from the design amplitude A due to the printing resolution. Besides possible printing uncertainties, asperity abrasion could also occur during transport and handling of the printed specimens. Moreover, during the mounting of specimens in the experimental devices, loose grains could deposit in the convex areas of the interface, which could prevent a complete interface contact and therefore reduce the effective amplitude from A to A_0. Given a printing resolution of 280 μm (corresponding to two grain diameters), we expect an error of the amplitude A in this range, which is quite high. Therefore, the most reliable way for estimating the amplitude A_0 for the interfaces designed herein is through Eq. (12).

Using the parameters presented in Table 2, we are able to calculate the expected friction behavior (Eq. (5)) and vertical displacement (Eq. (9)) of our laboratory experiments. The results of these calculations are presented in Figures 12, 13 and 14 together with the experimental curves. Notice that our main focus is on modeling the behavior after the first peak of friction. Before this point, in the loading branch, one could use a linear approximation for the shear force over shear displacement response and interpolate the vertical displacement.

Our model mimics very well the measured friction behavior with its oscillations. In addition, the vertical displacement (compaction/dilatancy) can be reproduced well, requiring only the identification of the overall compaction curve (red dashed line) as ad-

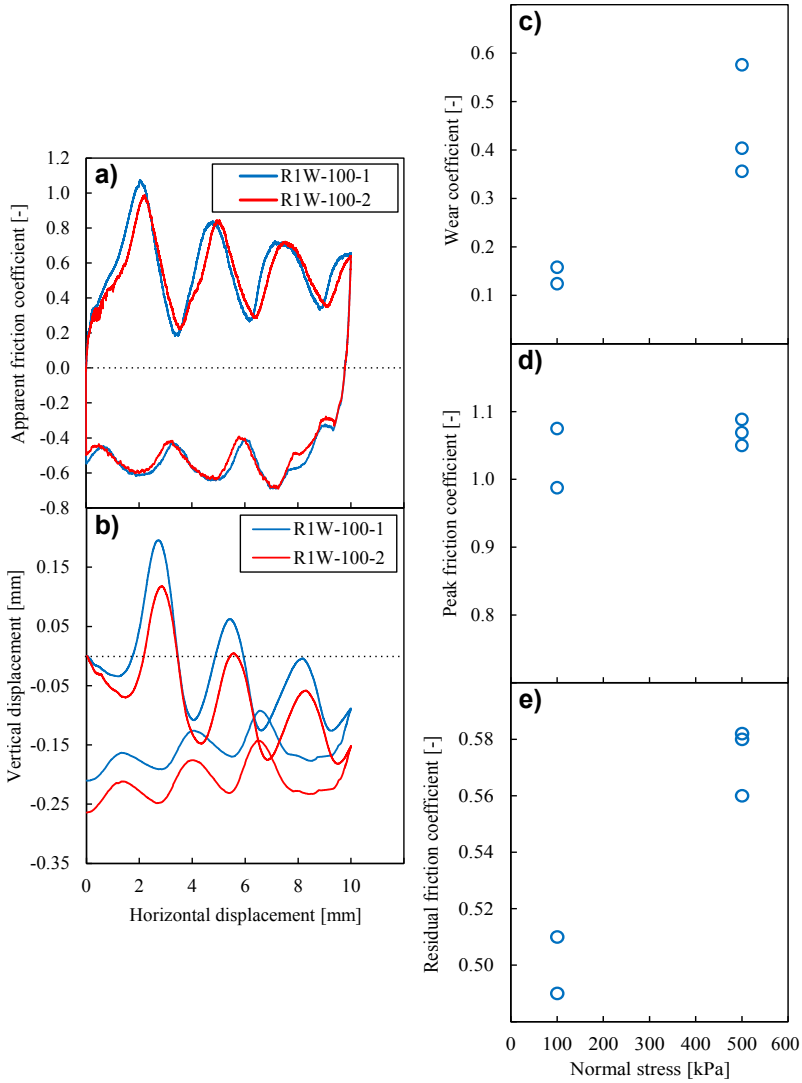

Figure 11. a), b) Friction experiments carried out on composition R1 under different 100 kPa of normal stress. c), d), e) Effect of normal stress on the friction characteristics: c) Wear coefficient, d) first peak friction and e) final friction of the abraded interface.

ditional model parameters. The additional oscillations (red solid line) are obtained from the relationships with the friction behavior, which confirm the model presented herein. As a result, this approach could be used for the design of interfaces of custom frictional properties (see Section 5).

5 Discussion

The presented experiments confirmed a good correspondence between the experimental behavior and our derived geometry-dependent friction law. The principal aspects and perspectives of this new method for creating analogue fault interfaces are discussed below.

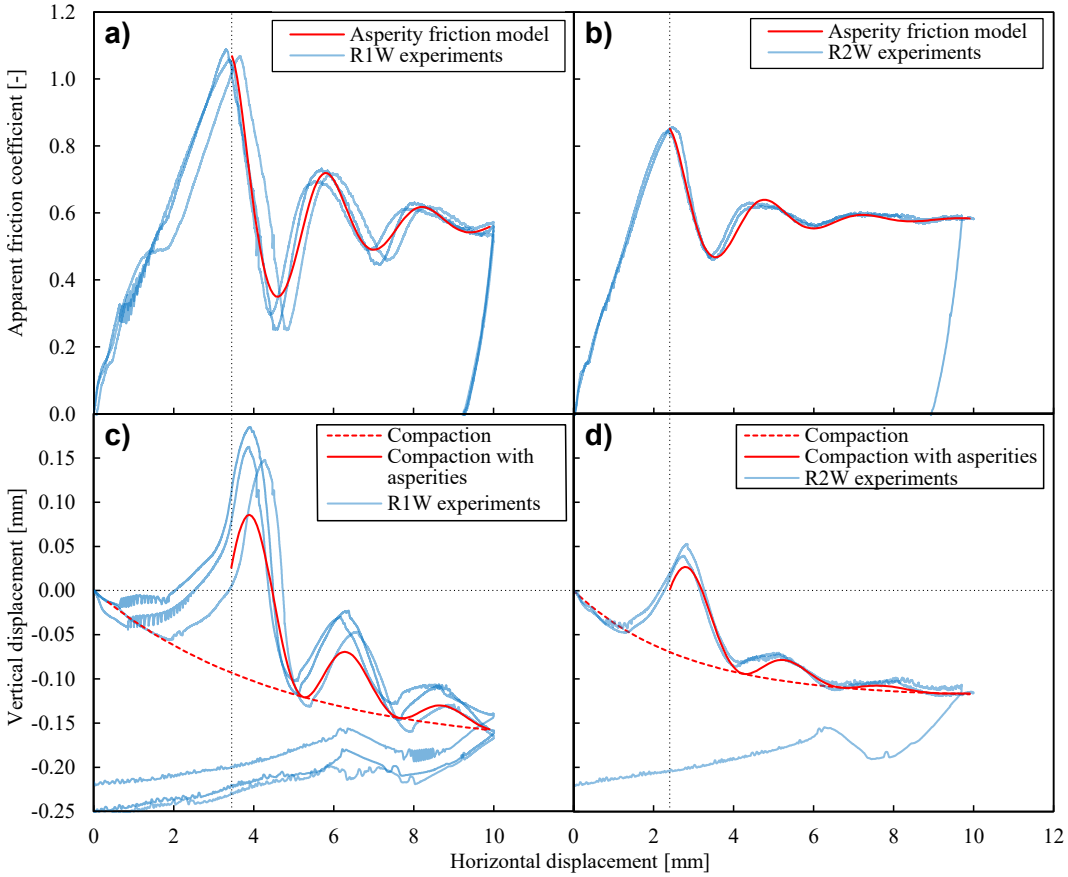

Figure 12. a), b) Evolution of friction and c), d) of vertical displacement with respect to the horizontal displacement, of R1 and R2 specimens under 500 kPa normal stress. The behavior calculated by our friction model (red solid lines) is compared with the experimental data (blue solid lines).

5.1 Frictional weakening

It is well-known how the stress drop (Noda et al., 2013) and the characteristic slip-weakening distance d_c^{sw} can lead to instabilities (see Figure 2 and also Dieterich, 1979; C. Scholz, 2002; Stefanou, 2019). Our surrogate experiments and model show that these properties can be adjusted by tuning the geometrical properties of the 3D-printed interfaces. For sinusoidal interfaces, we confirmed both theoretically and experimentally, that the characteristic slip distance d_c^{sw} is equivalent to half the asperity wavelength $d_c^{sw} = \lambda/2$ (see also Section 4.3). Using Eqs. (5) and (6), one can determine the friction drop $\Delta\mu = \mu(\delta_{pp} = \lambda/2) - \mu(\delta_{pp} = 0)$:

$$\Delta\mu = \left(1 + e^{-c_w \lambda/2}\right)\left(1 + \mu_b^2\right)\left[\frac{\lambda}{2\pi A_0} - \mu_b\left(1 + \frac{2\pi A_0}{\lambda}\right) + e^{-c_w\lambda/2}\mu_b\left(1 - \mu_b\frac{2\pi A_0}{\lambda}\right)\right]^{-1} \tag{13}$$

In case of no wear, Eq. (13) simplifies to:

$$\Delta\mu = \frac{4A_0\pi}{\lambda}\,\frac{1+\mu_b^2}{1 - 4\mu_b^2 A_0^2\pi^2\lambda^{-2}} \tag{14}$$

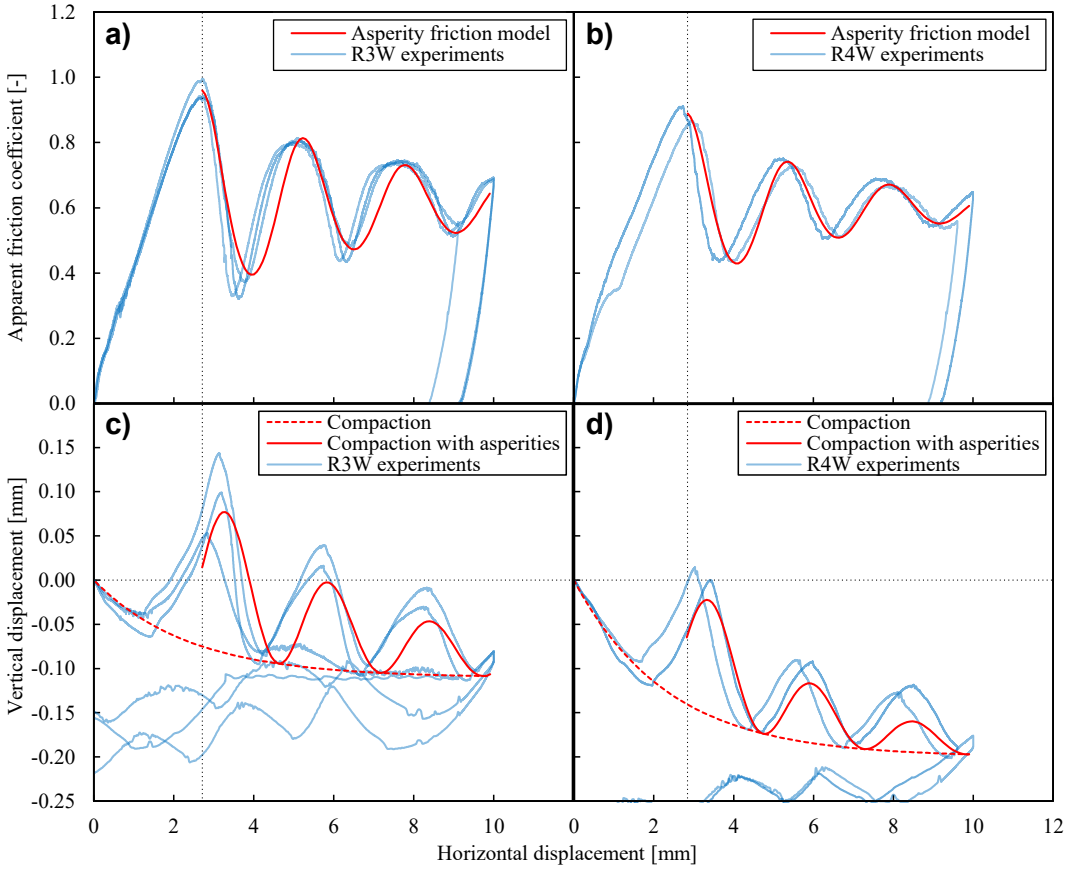

Figure 13. a), b) Evolution of friction and c), d) of vertical displacement with respect to the horizontal displacement, of R3 and R4 specimens under 500 kPa normal stress. The behavior calculated by our friction model (red solid lines) is compared with the experimental data (blue solid lines).

In addition, the slip-weakening slope, k_c, is highest at $\delta_{pp} = \lambda/4$, equal to (Eq. (5)):

$$k_c = -A_0 \frac{4\pi^2}{\lambda^2} \left(1 + \mu_b^2\right) \tag{15}$$

This slope is important for experiments focusing on reproducing the stick-slip behavior and earthquake-like events in the laboratory (see Section 2.4 and Dieterich (1978); Tinti et al. (2016); Scuderi et al. (2017); Stefanou (2019), among others).

Notice that by designing the roughness of the interfaces, we can adjust the slip-weakening behavior with great flexibility. Therefore, we are not limited by the intrinsic-fixed frictional properties (e.g. intrinsic rate-and-state friction) of the flat interfaces and we can design surrogate experiments with less constraints.

5.2 Wear, gouge production and dilatancy/compaction

Progressive sliding can influence the friction due to the wear of asperities, which is accompanied by gouge creation. The applied normal stress can have a non-negligible effect on the asperity wear. Higher normal stresses increase local shear and tensile stresses, which can lead to damage of the asperities and hence reduce the apparent friction. Our experiments showed that, while the material composition had a minor effect on the ini-

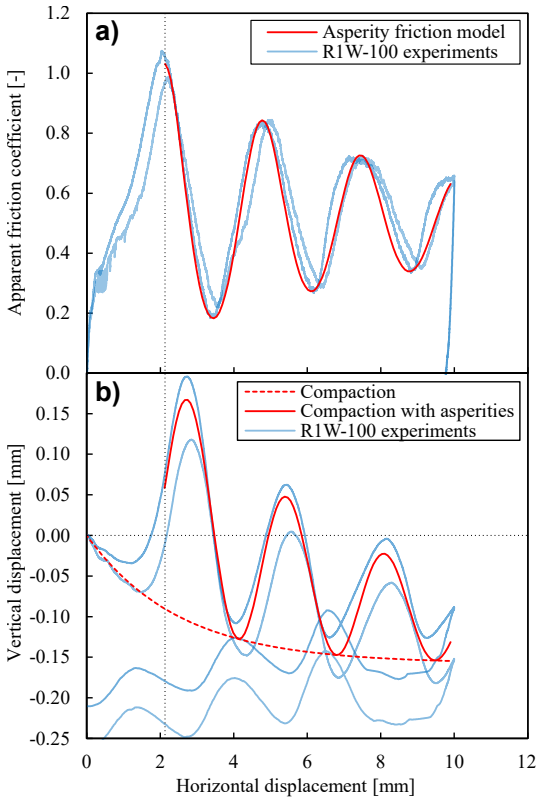

Figure 14. a) Evolution of friction and b) of vertical displacement with respect to the horizontal displacement, of R1 specimens under 100 kPa normal stress. The behavior calculated by our friction model (red solid lines) is compared with the experimental data (blue solid lines).

tial frictional behavior, it played a major role in wear. The resin binder is responsible for the material's tensile resistance and increased shear resistance due to grain bonding. Consequently, an increased binder content presumably reduces local failure of the asperities and preserves the designed and printed geometry of the interfaces.

In terms of dilatancy and compaction during shear, we observed a general compaction, accompanied by oscillating dilation due to the sinusoidal form of the interfaces tested herein. Wear is owed to the failure of the bonds between the grains, which progressively leads to the flattening of the interface, to the creation of gouge material and to compaction. The production of gouge material and compaction were evidenced by inspecting and weighting the specimens before and after shearing. The observed compaction reaches a constant value for large shear displacements, in accordance with the critical-state theory (Roscoe et al., 1958; Roscoe, 1970).

Notice that in their original state, the grains in the S3DP matrix have a very loose packing. After bond breakage, the grains are able to go into a denser packing causing a total volume reduction. Knowing the initial porosity (Table 1b), the measured vertical displacements $\delta_{v,\infty}$ (Table 2) and assuming a fault gouge density of 30%, we can roughly estimate the initial height of the damage/debonding zone. The thickness of this zone was equal to approximately $6D_{50}$. Due to denser packing at critical-state, this height reduces to approximately $4D_{50}$.

5.3 Fault instabilities in the laboratory and their control parameters

In order to transfer the behavior of an analogue experiment to the response of a real fault system, one has to employ scaling laws. By appropriate scaling of the lengths, the stresses, and the time (see Appendix A), one can simulate a real fault earthquake scenario in the laboratory. To this extent, the possibility of adjusting the frictional properties of the analogue fault interface as desired, gives a great flexibility for reproducing a wide spectrum of earthquake-like events in reduced scale in the laboratory.

As an example, we consider two idealized faults. The first one has a length of $L_{\mathrm{ac}}^{\mathrm{fault}} = 3$ km, while the second one has 7 times smaller length, namely $L_{\mathrm{ac}}^{\mathrm{fault}} = 0.43$ km. Both are ideally oriented for slip and share the same properties. In particular, both faults have $d_{\mathrm{c}}^{\mathrm{fault}}$ equal to 50 mm (see also Kanamori & Brodsky, 2004), an average in-situ effective normal stress $\sigma'^{\mathrm{fault}}_{\mathrm{n}}$ equal to 30 MPa that corresponds to a depth of 4-6 km, and an average shear stress drop $\Delta\tau^{\mathrm{fault}}$ of 3 MPa (cf. Sibson, 2011). The apparent shear modulus G^{fault} of the rocks surrounding the fault is constant and equal to 30 GPa. For these parameters, the first case of a fault would result to an earthquake event of $M_{\mathrm{w}} = 5.2$, while the second one would slide aseismically.

Based on the frictional properties of the surrogate material presented in this work, the above two scenarios could be represented by two differently printed interfaces of the R1 composition. The first one has the same wavelength $\lambda_1 = 2.8$ mm, as the one studied in Section 4.3, while the second one has a wavelength of $\lambda_2 = 19.6$ mm, which is 7 times larger. In order to provoke the seismic instability in an analogue manner, one has to add a spring of stiffness $k_{\mathrm{spr}}^{\mathrm{lab}} = 441$ N/mm, as shown schematically in Figure 2. Using the scaling laws that are summarized in the Appendix A and by applying an effective normal stress, $\sigma'^{\mathrm{lab}}_{\mathrm{n}}$, of 500 kPa over the printed interfaces of area 100×100 mm^2, the aforementioned idealized scenarios can be reproduced safely in the laboratory. Notice that the only difference in those tests is the geometry of the printed interfaces, i.e. the printed wavelength. Other adjustable model parameters could be the normal stress or the stiffness of the spring. However, being able to print the interfaces as desired gives an additional control parameter for the design of surrogate experiments. It is worth emphasizing that more complex configurations and tests could be conceptualized focusing also on the rupture propagation and slip direction along the printed curved interfaces following the studies of Marshall and Morris (2012); Romanet et al. (2020).

Moreover, the observed frictional oscillations due to the printed geometry could be used for imitating sequences of healing and rupture during the seismic cycle. More generally, the frictional properties of any printed (also non-sinusoidal) interface profile with recurring geometrical features are controlled through the maximum and minimum profile angles $i_{\max}$ and $i_{\min}$, the slip-weakening distance $d_{\mathrm{c}}^{\mathrm{sw}}$ and the "healing" distance d_{h} as shown in Figure 15. The maximum and minimum angles govern the peak and minimum friction, respectively. The distance $d_{\mathrm{c}}^{\mathrm{sw}}$ is equivalent to the displacement between the peak and the minimum friction (see also Figure 2b), while d_{h} defines the displacement from minimum to maximum friction. The sum $d_{\mathrm{c}}^{\mathrm{sw}}+d_{\mathrm{h}}$ denotes the total displacement between recurring friction peaks. By connecting these two points of given angles using splines, one can obtain the complete interface profile with controlled properties. This pattern would lead to events of custom magnitude and periodicity, contrary to the ones that would appear due to the rate-and-state frictional properties of the flat interfaces, which are intrinsic to a given material.

It is worth mentioning that in this study we investigated only interfaces with one (macro-) scale of asperities besides the micro-roughness owed to the grain-size. Our asperity scale was approaching the lower possible limit, due to the minimum printing resolution. Conversely, for larger asperity scales, the 3D-printing method is only limited by the printer's size, and different scales could be combined in one specimen. Moreover, we used only a 2D height profile, while one could print interfaces with 3D profiles, includ-

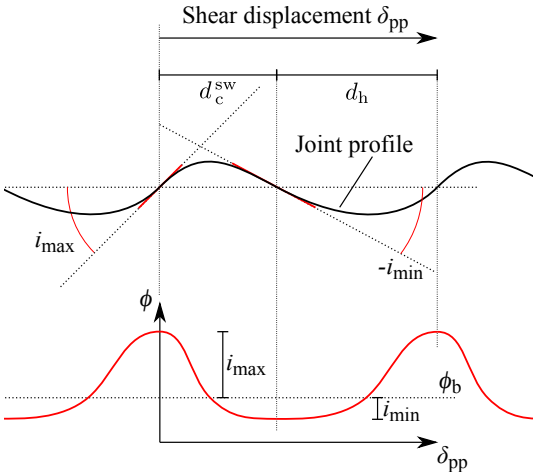

Figure 15. Schematic representation of a controlled joint friction behavior with adjustable maximum and minimum friction, slip and "healing" distance. Such interfaces could be used for mimicking earthquake cycles.

ing for instance fault patches with different properties or in-situ roughness (Kirkpatrick et al., 2020). In addition, the permeability of the material could be adjusted through microstructural modifications (Mitra, El Mansori, et al., 2019) and printing of flow channels (Head & Vanorio, 2016), which would allow one to carry out experiments with the presence of fluid and to simulate anthropogenic injections around the fault zone.

Other weakening mechanisms such as thermal pressurization, flash heating, melting or fluid injection at the fault were not considered in our approach and are worth of further investigation. These mechanisms could be potentially simulated in future experiments through fluid injection, heating, or shearing under high velocities and confinement, using the same or a modified S3DP material. Moreover, several effects, such as that of anisotropy, Poisson ratio, high confinement, porosity and fluid flow, to mention few, were not investigated in this work. Further works would be needed to address these issues.

6 Conclusions

Here we investigated, for the first time, the frictional properties of 3D sand-printed materials, which show a high potential for surrogate laboratory experiments involving frictional rock-like interfaces.

Pursuing further the works of Gomez (2017); Gomez et al. (2019), we performed detailed uniaxial compression tests, in order to identify the main bulk mechanical parameters of this new surrogate material. For instance we measured the Young modulus which varies from around 0.2 up to 3.7 GPa. These values are close to the ones of weak sandstones (e.g. Dobereiner & Freitas, 1986; Papamichos et al., 2000).

As far as it concerns the frictional properties, an apparent angle of friction of approximately 31° ($\mu \approx 0.6$) was determined based on direct-shear tests of flat sand-printed interfaces. This friction level is in the range of the friction angle of natural geomaterials and rock interfaces. The recoating speed and the binder saturation during printing showed to have a secondary role regarding the frictional behavior. However, these parameters did influence the creation of a thin gouge-like granular layer during shearing. Debonding of the granular particles are responsible for this thin layer, whose thickness was quantified in our experimental investigation.

The rate-and-state frictional parameters of flat 3D-printed interfaces were measured as well. It is worth mentioning that due to kinematics, the printed macro-roughness of other than flat interfaces was dominant over the measured rate-and-state frictional properties measured on the flat interfaces. Therefore, for the design and modeling of the frictional response of the S3DP specimens with wave interfaces, the slip-weakening friction law was adopted.

Furthermore, we showed how to adequately design the printed geometry of the sliding interfaces, in order to obtain custom a) maximum, minimum and residual apparent frictional properties, b) characteristic slip-weakening distance $d_{\mathrm{c}}^{\mathrm{sw}}$, c) evolution of friction coefficient with slip and d) dilatancy.

Experiments validated our design approach for achieving custom evolution of the apparent friction coefficient, which could be used to reproduce earthquake-like instabilities in the laboratory. Using adequate printing patterns, these earthquake-like instabilities could be designed to be periodic as well. Moreover, it is possible to control, to a certain extent, the creation of a gouge-like layer by modifying the geometry of the asperities and the binder content. This could provide tools for future studies on the influence of gouge on frictional properties.

According to the above, this printing method gives new perspectives for the design of surrogate experiments in fault mechanics. For this purpose, adequate scaling laws can be developed for performing analogue experiments in the laboratory. An example of such an experiment was described in this work. This kind of experiments could shed light on open scientific questions related to induced/triggered seismicity and its control (Stefanou, 2019, 2020). However, the use of this material is not limited in fault mechanics and can serve in other applications in geomechanics and geotechnics, such as tunneling, slope stability and landslides, among others.

Appendix A Scaling Laws for the S3DP material

Using scaling laws, one could upscale experimental results to real earthquake events. The parameters that we scale in this study are the displacement, the normal stress, the constitutive friction law and the time. The effective normal stress in the laboratory $\sigma'^{\,\mathrm{lab}}_{\mathrm{n}}$ is scaled by the dimensionless factor $\tilde{a}$:

$$\sigma'^{\,\mathrm{fault}}_{\mathrm{n}} = \tilde{a} \cdot \sigma'^{\,\mathrm{lab}}_{\mathrm{n}} \tag{A1}$$

The drop of the coefficient of friction $\Delta\mu^{\,\mathrm{lab}}$ is scaled by the dimensionless factor $\tilde{b}$:

$$\Delta\mu^{\,\mathrm{fault}} = \tilde{b} \cdot \Delta\mu^{\,\mathrm{lab}} \tag{A2}$$

Finally, the characteristic slip distance $d_{\mathrm{c}}^{\mathrm{lab}}$ is scaled by the dimensionless factor $\tilde{c}$:

$$d_{\mathrm{c}}^{\mathrm{fault}} = \tilde{c} \cdot d_{\mathrm{c}}^{\mathrm{lab}} \tag{A3}$$

Assuming slip-weakening frictional behavior (see Figure 2b), the normalized critical post-peak stiffness $\bar{k}_{\mathrm{c}}$ ($= k_{\mathrm{c}}/A$, where A is the area of the respective fault interface) of the S3DP material and the fault follows the same expression for both scales (Dieterich, 1979; C. Scholz, 2002; Stefanou, 2019):

$$\bar{k}_{\mathrm{c}} = \frac{\Delta\mu \cdot \sigma'_{\mathrm{n}}}{d_{\mathrm{c}}^{\mathrm{sw}}} \tag{A4}$$

If we combine Eqs. (A1)-(A5), we get the scaling relation between the normalized critical post-peak stiffness in the laboratory and in the in-situ scales:

$$\bar{k}_{\mathrm{c}}^{\,\mathrm{fault}} = \frac{\tilde{a}\cdot\tilde{b}}{\tilde{c}}\bar{k}_{\mathrm{c}}^{\,\mathrm{lab}} \tag{A5}$$

Analogously, we can scale the normalized elastic stiffness $\bar{k}$ ($= k/A$, where k is the stiffness of the spring) of the additional spring element (see Figure 2a) to the one of the rocks surrounding the fault:

$$\bar{k}^{\,\mathrm{fault}} = \frac{\tilde{a}\cdot\tilde{b}}{\tilde{c}}\bar{k}^{\,\mathrm{lab}} \tag{A6}$$

Consequently, the activated fault length $L_{\mathrm{ac}}^{\mathrm{fault}}$ can be calculated by the following expression (Dieterich, 1979, 1981b; C. Scholz, 2002):

$$L_{\mathrm{ac}}^{\mathrm{fault}} = \frac{G^{\mathrm{fault}}}{\bar{k}^{\,\mathrm{fault}}} \tag{A7}$$

where G^{fault} is the apparent shear modulus of the rock material. The basic instability condition of an analogue spring-slider model is given by $\bar{k} < \bar{k}_{\mathrm{c}}$ (Dieterich, 1978; C. Scholz, 2002; Stefanou, 2019). Therefore, by using the obtained laboratory data and the idealized dip-slip fault properties for both examined scenarios in Section 5.3, we get:

$$\#1: \qquad \bar{k}^{\,\mathrm{fault}} = 0.01\,\mathrm{MPa/mm} < \bar{k}_{\mathrm{c}}^{\,\mathrm{fault}} = 0.06\,\mathrm{MPa/mm} \tag{A8}$$

$$\#2: \qquad \bar{k}^{\,\mathrm{fault}} = 0.07\,\mathrm{MPa/mm} > \bar{k}_{\mathrm{c}}^{\,\mathrm{fault}} = 0.06\,\mathrm{MPa/mm} \tag{A9}$$

Using Eq. (A7), the #1 scenario corresponds to a fault with length $L_{\mathrm{ac},1}^{\mathrm{fault}} = 3$ km, while the #2 scenario to a fault with length $L_{\mathrm{ac},2}^{\mathrm{fault}} = 0.43$ km. As we can observe from Eqs. (A8) and (A9), only in the #1 case, we experience a dynamic instability. In the #2 case, the respective fault slips aseismically. The estimated earthquake magnitude of the nucleated instability of the #1 scenario can be derived by the following expression (Kanamori & Brodsky, 2004):

$$M_{\mathrm{w}} = \frac{2}{3}\log_{10} M_0 - 6.07 \tag{A10}$$

where M_0 is the seismic moment of the event in [Nm], with $M_0 \approx \Delta\tau^{\,\mathrm{fault}}\left(L_{\mathrm{ac}}^{\mathrm{fault}}\right)^3$ (Kanamori & Brodsky, 2004). Therefore, #1 fault scenario leads to an earthquake with magnitude $M_{\mathrm{w}} = 5.2$ (Eq. (A10)).

In addition, we can implicitly scale the characteristic time of the instability event by introducing an additional dimensionless scaling factor $\tilde{z}$ for the densities, as follows:

$$\rho^{\,\mathrm{fault}} = \tilde{z}\cdot\rho^{\,\mathrm{lab}} \tag{A11}$$

where $\rho^{\,\mathrm{fault}}$ represents the apparent density of the fault rocks and $\rho^{\,\mathrm{lab}}$ the density of the S3DP moving block. The characteristic time of the instability of the spring-slider can be given by:

$$t_{\,\mathrm{c}} = 2\pi\sqrt{\frac{m}{k}} \tag{A12}$$

where m is the mass of the equivalent sliding block. The mobilized mass of the surrounding rocks during the instability scales with $\left(L_{\mathrm{ac}}^{\,\mathrm{fault}}\right)^3$ and the density $\rho^{\,\mathrm{fault}}$ (Stefanou, 2019):

$$m^{\,\mathrm{fault}} = \varsigma \cdot \rho^{\,\mathrm{fault}} \cdot \left(L_{\mathrm{ac}}^{\,\mathrm{fault}}\right)^3 \tag{A13}$$

where ς is a shape factor which can be considered approximately equal to ~ 1. On the other hand, the mass of a S3DP block can be written as:

$$m^{\,\mathrm{lab}} = \rho^{\,\mathrm{lab}} \cdot A^{\,\mathrm{lab}} \cdot h^{\,\mathrm{lab}} \tag{A14}$$

where $A^{\,\mathrm{lab}}$ is the area of the frictional interface and $h^{\,\mathrm{lab}}$ is the height of the mobilized S3DP block (for parallelepiped blocks). Taking into account Eqs. (A6) and (A11)-(A14), one can derive the scaling relation of the characteristic fast time-scale of the system:

$$t_{\,\mathrm{c}}^{\,\mathrm{fault}} = \sqrt{\frac{\tilde{c} \cdot \tilde{z} \cdot L_{\mathrm{ac}}^{\,\mathrm{fault}}}{\tilde{a} \cdot \tilde{b} \cdot h^{\,\mathrm{lab}}}} \cdot t_{\,\mathrm{c}}^{\,\mathrm{lab}} \tag{A15}$$

For the distinction between the inherent fast and slow time-scales of the dynamics of the system we refer to Stefanou (2019).

Data Availability Statement

Data archiving is underway in https://svn.ec-nantes.fr/.

Acknowledgments

Funding: This work was supported by the European Research Council (ERC) under the European Union Horizon 2020 research and innovation program (Grant agreement no. 757848 CoQuake), *http://coquake.com*.

Contribution: All authors contributed to the analysis and writing the manuscript.

Competing interests: The authors declare that they have no competing interests.

References

Andrews, D. J. (1976). Rupture velocity of plane strain shear cracks. *Journal of Geophysical Research (1896-1977)*, *81*(32), 5679-5687. Retrieved from `https://agupubs.onlinelibrary.wiley.com/doi/abs/10.1029/JB081i032p05679` doi: 10.1029/JB081i032p05679

Anthony, J. L., & Marone, C. (2005). Influence of particle characteristics on granular friction. *Journal of Geophysical Research*, *110*(B08409), 1–14. doi: 10.1029/2004JB003399

Asadi, M. S., Rasouli, V., & Barla, G. (2013). A Laboratory Shear Cell Used for Simulation of Shear Strength and Asperity Degradation of Rough Rock Fractures. *Rock Mechanics and Rock Engineering*, *46*(4), 683–699. doi: 10.1007/s00603-012-0322-2

Barbot, S., Lapusta, N., & Avouac, J.-P. (2012). Under the Hood of the Earthquake Machine : Toward Predictive Modeling. *Science*, *336*(6082), 707–710. doi: 10.1126/science.1218796

Barton, N. (1973). Review of a new shear-strength criterion for rock joints. *Engineering Geology*, *7*(4), 287 - 332. Retrieved from http://www.sciencedirect.com/science/article/pii/0013795273900136 doi: https://doi.org/10.1016/0013-7952(73)90013-6

Bhattacharya, P., Rubin, A. M., Bayart, E., Savage, H. M., & Marone, C. (2015). Critical evaluation of state evolution laws in rate and state friction: Fitting large velocity steps in simulated fault gouge with time-, slip-, and stress-dependent constitutive laws. *Journal of Geophysical Research: Solid Earth*, *120*(9), 6365-6385. Retrieved from https://agupubs.onlinelibrary.wiley.com/doi/abs/10.1002/2015JB012437 doi: 10.1002/2015JB012437

Birch, F. (1966). Compressibility: Elastic constants. In P. S. CLARK (Ed.), *Handbook of physical constants* (97th ed., pp. 97–173). Geological Society of America.

Bommer, J. J., Oates, S., Cepeda, J. M., Lindholm, C., Bird, J., Torres, R., ... Rivas, J. (2006). Control of hazard due to seismicity induced by a hot fractured rock geothermal project. *Engineering Geology*, *83*(4), 287 - 306. Retrieved from http://www.sciencedirect.com/science/article/pii/S0013795205003108 doi: https://doi.org/10.1016/j.enggeo.2005.11.002

Brace, W. F., & Byerlee, J. D. (1966). Stick-slip as a mechanism for earthquakes. *Science*, *153*(3739), 990–992. Retrieved from https://science.sciencemag.org/content/153/3739/990 doi: 10.1126/science.153.3739.990

Brune, J. N. (1973). Earthquake modelling by stick-slip along precut surfaces in stressed foam rubber. *Bulletin of the Seismological Society of America*, *63*(6), 2105–2119. doi: 10.1016/0148-9062(74)90186-7

Candela, T., Renard, F., Klinger, Y., Mair, K., Schmittbuhl, J., & Brodsky, E. E. (2012). Roughness of fault surfaces over nine decades of length scales. *Journal of Geophysical Research: Solid Earth*, *117*(8), 1–30. doi: 10.1029/2011JB009041

Collins-Craft, N. A., Stefanou, I., Sulem, J., & Einav, I. (2020). A cosserat breakage mechanics model for brittle granular media. *Journal of the Mechanics and Physics of Solids*, *141*, 103975. Retrieved from http://www.sciencedirect.com/science/article/pii/S0022509620302106 doi: https://doi.org/10.1016/j.jmps.2020.103975

Dascher-Cousineau, K., Kirkpatrick, J. D., & Cooke, M. L. (2018). Smoothing of Fault Slip Surfaces by Scale-Invariant Wear. *Journal of Geophysical Research: Solid Earth*, *123*(9), 7913–7930. doi: 10.1029/2018JB015638

Dieterich, J. H. (1978). Time-dependent friction and the mechanics of stick-slip. *pure and applied geophysics*, *116*, 790–806. Retrieved from https://doi.org/10.1007/BF00876539 doi: 0.1007/BF00876539

Dieterich, J. H. (1979). Modeling of rock friction: 1. experimental results and constitutive equations. *Journal of Geophysical Research: Solid Earth*, *84*(B5), 2161-2168. Retrieved from https://agupubs.onlinelibrary.wiley.com/doi/abs/10.1029/JB084iB05p02161 doi: 10.1029/JB084iB05p02161

Dieterich, J. H. (1981a). Constitutive properties of faults with simulated gouge. In *Mechanical behavior of crustal rocks* (p. 103-120). American Geophysical Union (AGU). Retrieved from https://agupubs.onlinelibrary.wiley.com/doi/abs/10.1029/GM024p0103 doi: 10.1029/GM024p0103

Dieterich, J. H. (1981b). Potential for geophysical experiments in large scale tests. *Geophysical Research Letters*, *8*(7), 653-656. Retrieved from https://agupubs.onlinelibrary.wiley.com/doi/abs/10.1029/GL008i007p00653 doi: 10.1029/GL008i007p00653

Dieterich, J. H., & Kilgore, B. D. (1994, Mar 01). Direct observation of frictional contacts: New insights for state-dependent properties. *pure and applied geophysics*, *143*(1), 283-302. Retrieved from https://doi.org/10.1007/BF00874332 doi: 10.1007/BF00874332

Di Toro, G., Han, R., Hirose, T., De Paola, N., Nielsen, S., Mizoguchi, K., ... Shimamoto, T. (2011, Mar 01). Fault lubrication during earthquakes. *Nature*, *471*(7339), 494-498. Retrieved from https://doi.org/10.1038/nature09838 doi: 10.1038/nature09838

Dobereiner, L., & Freitas, M. H. D. (1986). Geotechnical properties of weak sandstones. *Géotechnique*, *36*(1), 79-94. Retrieved from https://doi.org/10.1680/geot.1986.36.1.79 doi: 10.1680/geot.1986.36.1.79

Edwards, B., Kraft, T., Cauzzi, C., Kästli, P., & Wiemer, S. (2015). Seismic monitoring and analysis of deep geothermal projects in St Gallen and Basel, Switzerland. *Geophysical Journal International*, *201*(2), 1022-1039. Retrieved from https://doi.org/10.1093/gji/ggv059 doi: 10.1093/gji/ggv059

Fang, Y., Elsworth, D., Ishibashi, T., & Zhang, F. (2018). Permeability Evolution and Frictional Stability of Fabricated Fractures With Specified Roughness. *Journal of Geophysical Research: Solid Earth*, *123*, 9355–9375. doi: 10.1029/2018JB016215

Farzadi, A., Waran, V., Solati-Hashjin, M., Rahman, Z. A. A., Asadi, M., & Osman, N. A. A. (2015). Effect of layer printing delay on mechanical properties and dimensional accuracy of 3D printed porous prototypes in bone tissue engineering. *Ceramics International*, *41*(7), 8320–8330. Retrieved from http://dx.doi.org/10.1016/j.ceramint.2015.03.004 doi: 10.1016/j.ceramint.2015.03.004

Gomez, J. S. (2017). *Mechanical Properties Characterization of Printed Reservoir Sandstone Analogues* (Master's thesis, University of Alberta). Retrieved from https://era.library.ualberta.ca/items/49660e82-3446-4a9a-9a74-e5ff2ab38470/download/7e82347e-42db-4031-bc32-12134e5441d7

Gomez, J. S., Chalaturnyk, R. J., & Zambrano-Narvaez, G. (2019). Experimental Investigation of the Mechanical Behavior and Permeability of 3D Printed Sandstone Analogues Under Triaxial Conditions. *Transport in Porous Media*, *129*(2), 541–557. Retrieved from https://doi.org/10.1007/s11242-018-1177-0 doi: 10.1007/s11242-018-1177-0

Goodman, R. E. (1989). *Introduction to rock mechanics* (Vol. 2). John Wiley & Sons.

Gu, J.-C., Rice, J. R., Ruina, A. L., & Tse, S. T. (1984). Slip motion and stability of a single degree of freedom elastic system with rate and state dependent friction. *Journal of the Mechanics and Physics of Solids*, *32*(3), 167 - 196. Retrieved from http://www.sciencedirect.com/science/article/pii/0022509684900073 doi: https://doi.org/10.1016/0022-5096(84)90007-3

Head, D., & Vanorio, T. (2016). Effects of changes in rock microstructures on permeability: 3-D printing investigation. *Geophysical Research Letters*, *43*(14), 7494–7502. doi: 10.1002/2016GL069334.Received

Heslot, F., Baumberger, T., Perrin, B., Caroli, B., & Caroli, C. (1994). Creep, stick-slip, and dry-friction dynamics: Experiments and a heuristic model. *Physical Review E*, *49*(6), 4973–4988. doi: 10.1103/PhysRevE.49.4973

Huang, T., Chang, C., & Chao, C. (2002). Experimental and mathematical modeling for fracture of rock joint with regular asperities. *Engineering Fracture Mechanics*, *69*(17), 1977 - 1996. Retrieved from http://www.sciencedirect.com/science/article/pii/S0013794402000723 doi: https://doi.org/10.1016/S0013-7944(02)00072-3

Hunfeld, L. B., Chen, J., Niemeijer, A. R., & Spiers, C. J. (2019). Temperature and gas/brine content affect seismogenic potential of simulated fault gouges derived from groningen gas field caprock. *Geochemistry, Geophysics, Geosystems*, *20*(6), 2827-2847. Retrieved from https://agupubs.onlinelibrary.wiley.com/doi/abs/10.1029/2019GC008221 doi: 10.1029/2019GC008221

Indraratna, B., Thirukumaran, S., Brown, E. T., & Zhu, S.-p. (2015). Modelling the Shear Behaviour of Rock Joints with Asperity Damage Under Constant

Normal Stiffness. *Rock Mechanics and Rock Engineering*, *48*, 179–195. doi: 10.1007/s00603-014-0556-2

Ishibashi, T., Fang, Y., Elsworth, D., Watanabe, N., & Asanuma, H. (2020). Hydromechanical properties of 3D printed fractures with controlled surface roughness : Insights into shear-permeability coupling processes. *International Journal of Rock Mechanics and Mining Sciences*, *128*(February), 104271. Retrieved from https://doi.org/10.1016/j.ijrmms.2020.104271 doi: 10.1016/j.ijrmms.2020.104271

Jeanne, P., Guglielmi, Y., Rutqvist, J., Nussbaum, C., & Birkholzer, J. (2017). Field characterization of elastic properties across a fault zone reactivated by fluid injection. *Journal of Geophysical Research: Solid Earth*, *122*(8), 6583–6598. doi: 10.1002/2017JB014384

Jones, L. (2018). *The big ones: How natural disasters have shaped us (and what we can do about them)*. Doubleday. (ISBN 978-178578-436-1)

Kanamori, H., & Brodsky, E. E. (2004). The physics of earthquakes. *Reports on Progress in Physics*, *67*(8), 1429–1496. doi: 10.1088/0034-4885/67/8/R03

King, C.-y. (1975). Model Seismicity and Faulting Parameters. *Bulletin of the Seismological Society of America*, *65*(1), 245–259.

Kirkpatrick, J. D., Edwards, J. H., Verdecchia, A., Kluesner, J. W., Harrington, R. M., & Silver, E. A. (2020). Subduction megathrust heterogeneity characterized from 3D seismic data. *Nature Geoscience*. Retrieved from http://dx.doi.org/10.1038/s41561-020-0562-9 doi: 10.1038/s41561-020-0562-9

Knuth, M., & Marone, C. (2007). Friction of sheared granular layers: Role of particle dimensionality, surface roughness, and material properties. *Geochemistry, Geophysics, Geosystems*, *8*(3). doi: 10.1029/2006GC001327

Li, Y., Oh, J., Mitra, R., & Hebblewhite, B. (2016). A constitutive model for a laboratory rock joint with multi-scale asperity degradation. *Computers and Geotechnics*, *72*, 143–151. doi: 10.1016/j.compgeo.2015.10.008

Marone, C. (1998). Laboratory-derived friction laws and their application to seismic faulting. *Annual Review of Earth and Planetary Sciences*, *26*(1), 643-696. Retrieved from https://doi.org/10.1146/annurev.earth.26.1.643 doi: 10.1146/annurev.earth.26.1.643

Marone, C., Raleigh, C. B., & Scholz, C. H. (1990). Frictional behavior and constitutive modeling of simulated fault gouge. *Journal of Geophysical Research: Solid Earth*, *95*(B5), 7007-7025. doi: 10.1029/JB095iB05p07007

Marone, C., & Scholz, C. (1989). Particle-size distribution and microstructures within simulated fault gouge. *Journal of Structural Geology*, *11*(7), 799 - 814. Retrieved from http://www.sciencedirect.com/science/article/pii/0191814189900990 (Friction phenomena in rock) doi: https://doi.org/10.1016/0191-8141(89)90099-0

Marshall, S. T., & Morris, A. C. (2012). Mechanics, slip behavior, and seismic potential of corrugated dip-slip faults. *Journal of Geophysical Research: Solid Earth*, *117*(B3). Retrieved from https://agupubs.onlinelibrary.wiley.com/doi/abs/10.1029/2011JB008642 doi: 10.1029/2011JB008642

Mitra, S., El Mansori, M., Rodríguez, A., Castro, D., & Costin, M. (2019). Study of the evolution of transport properties induced by additive processing sand mold using X-ray computed tomography. *Journal of Materials Processing Tech.*, *227*(116495), 1–15. Retrieved from https://doi.org/10.1016/j.jmatprotec.2019.116495 doi: 10.1016/j.jmatprotec.2019.116495

Mitra, S., Rodríguez de Castro, A., & El Mansori, M. (2018). The effect of ageing process on three-point bending strength and permeability of 3D printed sand molds. *International Journal of Advanced Manufacturing Technology*, *97*(1-4), 1241–1251. doi: 10.1007/s00170-018-2024-8

Mitra, S., Rodríguez de Castro, A., & El Mansori, M. (2019). On the rapid manufacturing process of functional 3D printed sand molds. *Journal of Manufacturing*

Processes, *42*(March), 202–212. Retrieved from https://doi.org/10.1016/j.jmapro.2019.04.034 doi: 10.1016/j.jmapro.2019.04.034

Newland, P. L., & Allely, B. H. (1957). Volume changes in drained taixial tests on granular materials. *Géotechnique*, *7*(1), 17-34. Retrieved from https://doi.org/10.1680/geot.1957.7.1.17 doi: 10.1680/geot.1957.7.1.17

Noda, H., Lapusta, N., & Kanamori, H. (2013, 03). Comparison of average stress drop measures for ruptures with heterogeneous stress change and implications for earthquake physics. *Geophysical Journal International*, *193*(3), 1691-1712. Retrieved from https://doi.org/10.1093/gji/ggt074 doi: 10.1093/gji/ggt074

Palmer, C., & Rice, J. R. (1973, April 03). The growth of slip surfaces in the progressive failure of over-consolidated clay. *Proceedings of The Royal Society A Mathematical Physical and Engineering Sciences*, *332*(1591), 527-548. doi: http://doi.org/10.1098/rspa.1973.0040

Papamichos, E., Tronvoll, J., Vardoulakis, I., Labuz, J. F., Skjærstein, A., Unander, T. E., & Sulem, J. (2000). Constitutive testing of Red Wildmoor sandstone. *Mechanics of Cohesive-Frictional Materials*, *5*, 1–40. doi: 10.1002/(SICI)1099-1484(200001)5

Patton, F. D. (1966). Multiple modes of shear failure in rock. In *Proc. 1st congr. int. soc. rock mech.* (pp. 509–513). Lisbon. Retrieved from https://www.onepetro.org/conference-paper/ISRM-1CONGRESS-1966-087

Pimienta, L., Fortin, J., & Guéguen, Y. (2015). Experimental study of Young's modulus dispersion and attenuation in fully saturated sandstones. *Geophysics*, *80*(5), L57-L72. Retrieved from https://doi.org/10.1190/geo2014-0532.1 doi: 10.1190/geo2014-0532.1

Popov, V. L., Grzemba, B., Starcevic, J., & Popov, M. (2012). Rate and state dependent friction laws and the prediction of earthquakes: What can we learn from laboratory models? *Tectonophysics*, *532-535*, 291–300. doi: 10.1016/j.tecto.2012.02.020

Power, W. L., Tullis, T. E., & Weeks, J. D. (1988). Roughness and wear during brittle faulting. *Journal of Geophysical Research: Solid Earth*, *93*(B12), 15268-15278. Retrieved from https://agupubs.onlinelibrary.wiley.com/doi/abs/10.1029/JB093iB12p15268 doi: 10.1029/JB093iB12p15268

Primkulov, B., Chalaturnyk, J., Chalaturnyk, R., & Narvaez, G. Z. (2017). 3D Printed Sandstone Strength : Curing of Furfuryl Alcohol Resin-Based Sandstones. *3D Printing and Additive Manufacturing*, *4*(3), 149–155. doi: 10.1089/3dp.2017.0032

Queener, C., Smith, T., & Mitchell, W. (1965). Transient wear of machine parts. *Wear*, *8*(5), 391 - 400. Retrieved from http://www.sciencedirect.com/science/article/pii/0043164865901705 doi: https://doi.org/10.1016/0043-1648(65)90170-5

Rabinowicz, E. (1951). The nature of the static and kinetic coefficients of friction. *Journal of Applied Physics*, *22*(11), 1373–1379. doi: 10.1063/1.1699869

Rabinowicz, E. (1956). Stick and slip. *Scientific American*, *194*(5), 109–119. Retrieved from http://www.jstor.org/stable/26122743

Rabinowicz, E. (1958). The intrinsic variables affecting the stick-slip process. *Proceedings of the Physical Society*, *71*(4), 668–675. doi: 10.1088/0370-1328/71/4/316

Raleigh, C. B., Healy, J. H., & Bredehoeft, J. D. (1976). An Experiment in Earthquake Control at Rangely, Colorado. *Science*, *191*(4233), 1230–1237. Retrieved from http://www.sciencemag.org/cgi/doi/10.1126/science.191.4233.1230 doi: 10.1126/science.191.4233.1230

Rattez, H., Stefanou, I., & Sulem, J. (2018a). The importance of Thermo-Hydro-Mechanical couplings and microstructure to strain localization in 3D continua with application to seismic faults. Part I: Theory and linear stability

analysis. *Journal of the Mechanics and Physics of Solids*, *115*(March), 54–76. Retrieved from https://linkinghub.elsevier.com/retrieve/pii/S0022509617309626 doi: 10.1016/j.jmps.2018.03.004

Rattez, H., Stefanou, I., Sulem, J., Veveakis, M., & Poulet, T. (2018b). The importance of Thermo-Hydro-Mechanical couplings and microstructure to strain localization in 3D continua with application to seismic faults. Part II: Numerical implementation and post-bifurcation analysis. *Journal of the Mechanics and Physics of Solids*, *115*, 1–29. Retrieved from https://linkinghub.elsevier.com/retrieve/pii/S0022509617309638 doi: 10.1016/j.jmps.2018.03.003

Reches, Z., & Lockner, D. A. (2010, Sep 01). Fault weakening and earthquake instability by powder lubrication. *Nature*, *467*(7314), 452-455. Retrieved from https://doi.org/10.1038/nature09348 doi: 10.1038/nature09348

Rice, J. R. (2017). Heating, weakening and shear localization in earthquake rupture. *Philosophical Transactions of the Royal Society A: Mathematical, Physical and Engineering Sciences*, *375*(2103), 20160015. Retrieved from https://royalsocietypublishing.org/doi/abs/10.1098/rsta.2016.0015 doi: 10.1098/rsta.2016.0015

Rice, J. R., Rudnicki, J. W., & Platt, J. D. (2014). Stability and localization of rapid shear in fluid-saturated fault gouge: 1. linearized stability analysis. *Journal of Geophysical Research: Solid Earth*, *119*(5), 4311-4333. Retrieved from https://agupubs.onlinelibrary.wiley.com/doi/abs/10.1002/2013JB010710 doi: 10.1002/2013JB010710

Rice, J. R., & Ruina, A. L. (1983, 06). Stability of Steady Frictional Slipping. *Journal of Applied Mechanics*, *50*(2), 343-349. Retrieved from https://doi.org/10.1115/1.3167042 doi: 10.1115/1.3167042

Romanet, P., Sato, D. S., & Ando, R. (2020, 06). Curvature, a mechanical link between the geometrical complexities of a fault: application to bends, kinks and rough faults. *Geophysical Journal International*, *223*(1), 211-232. Retrieved from https://doi.org/10.1093/gji/ggaa308 doi: 10.1093/gji/ggaa308

Roscoe, K. H. (1970). The influence of strains in soil mechanics. *Géotechnique*, *20*(2), 129-170. Retrieved from https://doi.org/10.1680/geot.1970.20.2.129 doi: 10.1680/geot.1970.20.2.129

Roscoe, K. H., Schofield, A. N., & Wroth, C. P. (1958). On the yielding of soils. *Géotechnique*, *8*(1), 22-53. Retrieved from https://doi.org/10.1680/geot.1958.8.1.22 doi: 10.1680/geot.1958.8.1.22

Rosenau, M., Corbi, F., & Dominguez, S. (2017). Analogue earthquakes and seismic cycles: experimental modelling across timescales. *Solid Earth*, *8*(3), 597-635. Retrieved from https://hal.archives-ouvertes.fr/hal-01553120 doi: 10.5194/se-8-597-2017

Ruina, A. (1983). Slip instability and state variable friction laws. *Journal of Geophysical Research: Solid Earth*, *88*(B12), 10359-10370. Retrieved from https://agupubs.onlinelibrary.wiley.com/doi/abs/10.1029/JB088iB12p10359 doi: 10.1029/JB088iB12p10359

Sammis, C. G., Lockner, D. A., & Reches, Z. (2011, Dec 01). The role of adsorbed water on the friction of a layer of submicron particles. *Pure and Applied Geophysics*, *168*(12), 2325-2334. Retrieved from https://doi.org/10.1007/s00024-011-0324-0 doi: 10.1007/s00024-011-0324-0

Schallamach, A. (1971). How does rubber slide? *Wear*, *17*(4), 301 - 312. Retrieved from http://www.sciencedirect.com/science/article/pii/0043164871900330 doi: https://doi.org/10.1016/0043-1648(71)90033-0

Schmittbuhl, J., Gentier, S., & Roux, S. (1993). Field measurements of the roughness of fault surfaces. *Geophysical Research Letters*, *20*(8), 639–641. doi: 10.1029/93GL00170

Scholz. (1998, Jan 01). Earthquakes and friction laws. *Nature*, *391*(6662), 37-42. Re-

trieved from https://doi.org/10.1038/34097 doi: 10.1038/34097

Scholz, C. (2002). *The Mechanics of Earthquakes and Faulting* (2nd ed.). New York: Cambridge University Press. doi: 10.1017/CBO9780511818516

Schön, J. H. (2004). *Physical properties of rocks: Fundamentals and principles of petrophysics*. Elsevier.

Schumacher, M., Deisinger, U., Detsch, R., & Ziegler, G. (2010). Indirect rapid prototyping of biphasic calcium phosphate scaffolds as bone substitutes : influence of phase composition , macroporosity and pore geometry on mechanical properties. *Journal of Materials Science: Materials in Medicine*, *21*, 3119–3127. doi: 10.1007/s10856-010-4166-6

Scuderi, M. M., Collettini, C., & Marone, C. (2017). Frictional stability and earthquake triggering during fluid pressure stimulation of an experimental fault. *Earth and Planetary Science Letters*, *477*, 84–96. doi: 10.1016/j.epsl.2017.08.009

Scuderi, M. M., Marone, C., Tinti, E., Di Stefano, G., & Collettini, C. (2016). Precursory changes in seismic velocity for the spectrum of earthquake failure modes. *Nature Geoscience*, *9*(9), 695–700. doi: 10.1038/ngeo2775

Sibson, R. H. (2011, 01). The scope of earthquake geology. In *Geology of the Earthquake Source: A Volume in Honour of Rick Sibson.* Geological Society of London. Retrieved from https://doi.org/10.1144/SP359.18 doi: 10.1144/SP359.18

Stefanou, I. (2019). Controlling anthropogenic and natural seismicity: Insights from active stabilization of the spring-slider model. *Journal of Geophysical Research: Solid Earth*, *124*(8), 8786-8802. Retrieved from https://agupubs.onlinelibrary.wiley.com/doi/abs/10.1029/2019JB017847 doi: 10.1029/2019JB017847

Stefanou, I. (2020). Control Self-Organized Critical behavior and incite slow-slip in generalized Burridge-Knopoff models. *submitted for publication*.

Tinti, E., Scuderi, M. M., Scognamiglio, L., Di Stefano, G., Marone, C., & Collettini, C. (2016). On the evolution of elastic properties during laboratory stick-slip experiments spanning the transition from slow slip to dynamic rupture. *Journal of Geophysical Research: Solid Earth*, *121*(12), 8569-8594. Retrieved from https://agupubs.onlinelibrary.wiley.com/doi/abs/10.1002/2016JB013545 doi: 10.1002/2016JB013545

Tzortzopoulos, G., Braun, P., & Stefanou, I. (2020). Absorbent porous paper reveals how earthquakes could be mitigated. *submitted to Geophysical Research Letters, manuscript 2020GL090792*.

Tzortzopoulos, G., Stefanou, I., & Braun, P. (2019). Designing Experiments for Controlling earthQuakes (CoQuake) by Fluid Injection. In *12th hstam 2019 international congress on mechanics.* Thessaloniki, Greece.

Upadhyay, M., Sivarupan, T., & El Mansori, M. (2017). 3D printing for rapid sand casting—A review. *Journal of Manufacturing Processes*, *29*, 211–220. Retrieved from http://dx.doi.org/10.1016/j.jmapro.2017.07.017 doi: 10.1016/j.jmapro.2017.07.017

Vaezi, M., & Chua, C. K. (2011). Effects of layer thickness and binder saturation level parameters on 3D printing process. *The International Journal of Advanced Manufacturing Technology*, *53*, 275–284. doi: 10.1007/s00170-010-2821-1

Viesca, R. C., & Garagash, D. I. (2015, Nov 01). Ubiquitous weakening of faults due to thermal pressurization. *Nature Geoscience*, *8*(11), 875-879. Retrieved from https://doi.org/10.1038/ngeo2554 doi: 10.1038/ngeo2554

Vlasea, M., Pilliar, R., & Toyserkani, E. (2015). Control of Structural and Mechanical Properties in Bioceramic Bone Substitutes via Additive Manufacturing Layer Stacking Orientation. *Additive Manufacturing*, *6*, 30–38. Retrieved from http://dx.doi.org/10.1016/j.addma.2015.03.001 doi:

10.1016/j.addma.2015.03.001

Wood, D. M. (1991). Plasticity and yielding. In *Soil behaviour and critical state soil mechanics* (p. 55–83). Cambridge University Press. doi: 10.1017/CBO9781139878272.004